Biophysical Journal
Article

Biophysical Society

On multistability and constitutive relations of cell motion on fibronectin lanes

Behnam Amiri,[1] Johannes C. J. Heyn,[2] Christoph Schreiber,[2] Joachim O. Rädler,[2,*] and Martin Falcke[1,3,*]
[1]Max Delbrück Center for Molecular Medicine in the Helmholtz Association, Berlin, Germany; [2]Fakultät für Physik, Ludwig-Maximilians-Universität München (LMU), Munich, Germany; and [3]Department of Physics, Humboldt University, Berlin, Germany

ABSTRACT Cell motility on flat substrates exhibits coexisting steady and oscillatory morphodynamics, the biphasic adhesion-velocity relation, and the universal correlation between speed and persistence (UCSP) as simultaneous observations common to many cell types. Their universality and concurrency suggest a unifying mechanism causing all three of them. Stick-slip models for cells on one-dimensional lanes suggest multistability to arise from the nonlinear friction of retrograde flow. This study suggests a mechanical mechanism controlled by integrin signaling on the basis of a biophysical model and analysis of trajectories of MDA-MB-231 cells on fibronectin lanes, which additionally explains the constitutive relations. The experiments exhibit cells with steady or oscillatory morphodynamics and either spread or moving with spontaneous transitions between the dynamic regimes, spread and moving, and spontaneous direction reversals. Our biophysical model is based on the force balance at the protrusion edge, the noisy clutch of retrograde flow, and a response function of friction and membrane drag to integrin signaling. The theory reproduces the experimentally observed cell states, characteristics of oscillations, and state probabilities. Analysis of experiments with the biophysical model establishes a stick-slip oscillation mechanism, and explains multistability of cell states and the statistics of state transitions. It suggests protrusion competition to cause direction reversal events, the statistics of which explain the UCSP. The effect of integrin signaling on drag and friction explains the adhesion-velocity relation and cell behavior at fibronectin density steps. The dynamics of our mechanism are nonlinear flow mechanics driven by F-actin polymerization and shaped by the noisy clutch of retrograde flow friction, protrusion competition via membrane tension, and drag forces. Integrin signaling controls the parameters of the mechanical system.

SIGNIFICANCE Biophysical comprehension of cell motion and morphodynamics means to characterize them experimentally and explain them based on the internal cell dynamics. We characterize motion of MDA-MB-231 cells by analyzing 29,500 trajectories on one-dimensional fibronectin lanes. We suggest the intrinsic dynamics to derive from three constituents, namely the protrusion edge force balance, the noisy clutch mechanism of retrograde flow, and integrin signaling. Corresponding theory reproduces the measured morphodynamics. It also captures the measured motion characteristics given as the constitutive adhesion-velocity relation and persistence-speed relation and its response to drugs. We predict the constitutive force-velocity relation. Hence, the constituents of the mechanism, which apply to many cell types, explain the complex morphodynamics and constitutive motion relations.

INTRODUCTION

The motion of eukaryotic cells is essential for embryonic development, wound healing, immune responses, and tumor metastasis (1). Much effort has been devoted to the study of mesenchymal migration with prototypical in vitro motion of cells on two-dimensional (2D) adhesive substrates. Cell migration starts with polarization breaking the spatial symmetry and the formation of a lamellipodium, which is a protrusion of a thin sheet of cytoplasm (0.1–0.3 μm thick) covering tens to hundreds of square micrometers (2–7). The lamellipodium is mechanically stabilized by adhesion with the substrate (8–14) and is constructed from a network of actin filaments (15–19). Polymerization of filament barbed ends at the leading edge of the lamellipodium generates motion and pushes the edge forward (20–23). Further back, the pointed ends depolymerize and replenish the pool of actin monomers (18,19). Once cells are moving, their shape is

Submitted October 21, 2022, and accepted for publication January 31, 2023.

*Correspondence: raedler@lmu.de or martin.falcke@mdc-berlin.de

Editor: Dimitrios Vavylonis.

https://doi.org/10.1016/j.bpj.2023.02.001

determined by internal force-generation patterns and adhesion (24–29).

Many cell types obey both the adhesion-velocity relation and the universal correlation between speed and persistence (UCSP). The dependency of the cell velocity on adhesion exhibits a velocity maximum at intermediate strength, and slower velocities both at weak and strong adhesion (10–14,26,30–35). Results on the UCSP, describing the relation between cell velocity and persistence time, suggest it to be of similar universality (36). The faster cells move, the more persistent they move. Maiuri et al. report this observation for many different cell types and suggest persistence time to depend exponentially on cell velocity (36). These types of relations describing the response of a system to external parameters are called constitutive relations in the fields of physics and engineering. The stationary force-velocity relation is another constitutive relation we will discuss.

Another general observation is that both the shape and the motile state of cells are highly dynamic. Cells stop and start to move again, develop new protrusions, and change direction (25,29,37–53). In addition to these states of motion, there exist states distinguished by the dynamic regime of front protrusion and cell back and/or back protrusion. Stationary and oscillatory dynamic regimes with one or several protrusions have been observed and have caused a surge of interest in multistability in cell motility (5,47,51,52,54–62).

Multistability with its state dynamics, biphasic adhesion-velocity relation, and the UCSP appear to describe the motile behavior of many different cell types. Mechanisms have been suggested for multistability (47,56,57,59–62), the biphasic adhesion-velocity relation (11,31,34,35), the UCSP (36), and the stationary force-velocity relation (63), each separately. However, the generality and concurrency of multistability and the constitutive relations strongly suggest that a single mechanism should explain all three of them.

In search for such a mechanism, we carry out a series of experiments with MDA-MB-231 cells on one-dimensional (1D) lanes in a range of fibronectin concentrations and formulate our suggestion for a mechanism as a biophysical model based on previous studies (35,64). The mechanism involves the force balance at the protrusion edges, the clutch mechanism of retrograde flow, competing protrusions, and integrin signaling. Our key finding is that the intracellular dynamics generating multistability also determine the constitutive relations. We introduce basic experimental observations in the section "dynamic cell states," characterize cell states and compare experimental and simulated data in "analysis of dynamic cell states," and explain state transitions and their relation to the UCSP in "transitions between cell states." We explain the ideas defining the theory and compute the force-velocity relation and adhesion-velocity relation in materials and methods.

MATERIALS AND METHODS

Cell culture

We cultured MDA-MB-231 breast cancer cells stably transduced with histone-2B mCherry (gift from Timo Betz, WWU Münster, Germany) in L15 medium with 2 mM Glutamax (Thermo Fisher Scientific, Waltham, MA, USA) plus 10% fetal bovine serum (Thermo Fisher) at 37°C. Cells were passaged every 2–3 days using Accutase (Thermo Fisher). For experiments, about 5000 cells were seeded per dish. After 2–3 h, cells adhered to the micropatterns and we exchanged the medium to L15 medium without phenol red. We then transferred the samples to the microscope and started measurements within 1–2 h. For inhibitor experiments 10 μM (+/−)-blebbistatin (Cayman Chemical, Ann Arbor, MI, USA), 100 nM latrunculin A (Merck, Darmstadt, Germany), or 0.25 nM calyculin A (Thermo Fisher) were added 2 h before the start of the experiment. As control we used dimethyl sulfoxide (Life Technologies, Darmstadt, Germany) equal to the amount used for the dilution of the inhibitors.

Micropatterning

Lanes (15 μm wide) which were homogeneously coated with fibronectin (FN) (YO Proteins, Ronninge, Sweden) were applied on an imaging dish with a polymer coverslip bottom (ibidi, Gräfelfing, Germany) using a microcontact printing protocol. The production of the polydimethylsiloxane stamps and the subsequent printing has been described previously (65). For all experiments, a range of FN densities was covered.

Determination of fibronectin densities

We determined the FN density via fluorescence intensity as described previously by our group (35). Lyophilized FN batches were resuspended and conjugated with Alexa Fluor 647 NHS ester (Thermo Fisher). We measured the concentration of FN in solution by optical absorption at 280 nm (Nanodrop, Thermo Fisher). The calibration factor that enables the conversion of fluorescence intensity to FN density was determined using microfluidic channel slides that were filled with an FN solution of known concentration.

Microscopy

We performed time-lapse imaging on an inverted fluorescence microscope (Nikon Eclipse Ti, Nikon, Tokyo, Japan) equipped with an XY-motorized stage, Perfect Focus System (Nikon), and a heating chamber (Okolab, Pozzuoli, Italy) set to 37°C. Arrays of fields of view were sequentially scanned and imaged using the motorized stage, the Perfect Focus System, a 10× CFI Plan Fluor DL objective (Nikon), a CMOS camera (PCO edge 4.2, Excelitas PCO, Kelheim, Germany) and the acquisition software NIS Elements (Nikon). Before the start of the time-lapse measurement, epifluorescence images of the FN patterns were taken. Phase-contrast images of the cells and epifluorescence images of their nuclei were then taken for 48 h at 10-min or 30-s intervals as indicated. Intervals of 10 min allowed scanning of $12 \times 12 = 144$ fields of view, while intervals of 30 s allowed $4 \times 4 = 16$ fields of view.

Image analysis

Image analysis was performed using a combination of MATLAB R2020a (MathWorks, Natick, MA, USA) scripts and FIJI (ImageJ) macros, based on previous work (35). FN lanes are detected using a Hough transformation of the fluorescence signal of the labeled FN. The position of the nuclei is tracked by setting a threshold after applying a background correction and band-pass filter to the fluorescent images of the nuclei. The coordinates of the nuclei are converted such that the x coordinates are parallel to the FN lanes. The position of the front and back of the cells is determined

via kymographs that are created along the center of the FN lane. The cell edge is then manually segmented. Code used to generate results in the current study is available on GitHub: https://github.com/behnam89amiri/Multistability_and_constitutive_relations_of_cell_motion.

Biophysical model

We define here the model constituents and their rate laws. This will result in differential equations for the protrusion lengths $L_{f,b}$ and friction coefficients $\kappa_{f,b}$ for the front (f) and back (b) protrusions. Protrusion edge velocities $v_{f,b}$, cell body velocity v_c, retrograde flow velocities $v_{rf}, v_{r,b}$, and protrusion edge forces $F_{f,b}$ are determined by algebraic equations of $L_{f,b}$ and $\kappa_{f,b}$, all listed in the supporting material. Algebraic equations also relate the parameters of these dynamics to integrin signaling and the FN density.

Motivated by the observations presented in Fig. 1, we formulate a cell model with front and back protrusions moving on a 1D FN lane (Fig. 2 *A*). The model is based in part on our previous work on steady cell motion by Schreiber et al. (35). The main extensions of the model compared with Schreiber et al. (35) are the cell body, the back protrusion, and the noisy clutch. The requirement for the noisy clutch from a modeling point of view follows from the dynamics we consider here, while we considered stationary properties in (35).

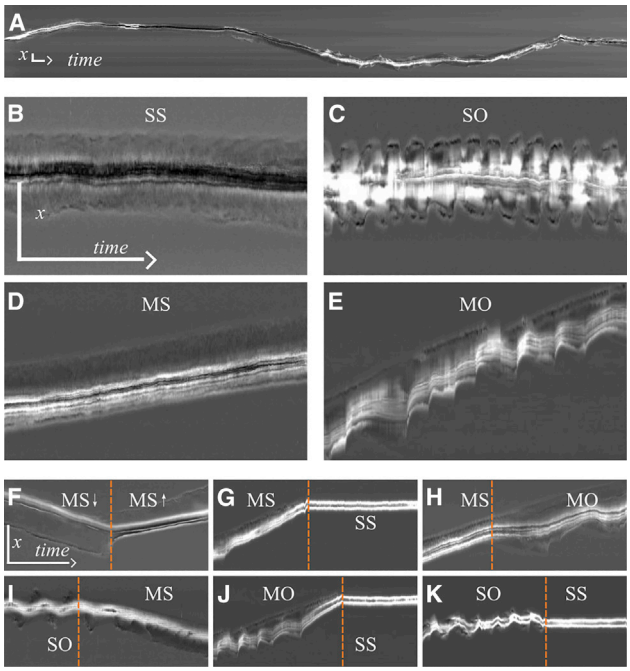

FIGURE 1 Four dynamic states and two motion directions form the multistability of MDA-MB-231 cells on homogeneous fibronectin lanes. (*A*) Kymograph from a typical 48-h trajectory. (*B*) A spread (S) cell with steady length (S). We call this state SS. (*C*) A spread cell with oscillatory length (O). We call this state SO. (*D*) A moving cell (M) with steady length: state MS. (*E*) A moving cell with oscillating length: state MO. (*F*) Transition from a downward-moving MS state to an upward-moving MS state. (*G–K*) The cells undergo an MS → SS (*G*), MS → MO (*H*), SO → MS (*I*), MO → SS (*J*), and SO → SS (*K*) transition. Vertical orange lines indicate the point in time of the state transitions as determined by the change point algorithm described in section S2. All kymographs are shown with a time resolution of 30 s. Time goes from left to right. The vertical scale bars represent 100 μm, the horizontal scale bars 60 min. The scale bars in (*B*) apply to (*B–E*), and the scale bars in (*F*) apply to (*F–K*). The movies corresponding to kymographs (*A–F*) can be found in the supporting material. To see this figure in color, go online.

The force balances (see Eqs. S2–S4 and Fig. 2 *A*) applied to the front and back edges and cell body have been established in a variety of studies (20–22,63,66–69). They comprise the drag forces resisting motion $\zeta_{f,b}v_{f,b}$ and $\zeta_c v_c$, the retrograde flow friction force $\kappa_{f,b}v_{r,f,b}$, and the elastic forces (Fig. 2 *A*). The drag coefficients $\zeta_{f,b,c}$ and the retrograde flow friction coefficients $\kappa_{f,b}$ are affected by adhesion and integrin signaling (Eqs. 2, 3, S17, and S18). The cell body velocity v_c is determined by the forces acting on it from front and back protrusions and the drag coefficient of the cell body ζ_c.

We choose a linear dependency of the force between protrusion edges and cell body on the protrusion length (elastic force) based on the results in (35) (see Eqs. S2–S4 and (51)). We assume that the force is transmitted by membrane tension and consider as its most likely cause volume homeostasis in 1D (70).

The network extension rate v_e is equal to the vectorial difference of the edge velocity and retrograde flow velocity. It is fixed by polymerization, which is force dependent with the well-known Arrhenius factor (66,68,71) (see Eqs. S5 and S6).

The lengths of the protrusions $L_{f,b}$ are dynamic due to velocity differences between the edges and the cell body:

$$\frac{dL_f}{dt} = v_f - v_c, \frac{dL_b}{dt} = v_c - v_b. \tag{1}$$

The noisy clutch has been reported in a variety of studies (64,72–79) and is due to the retrograde motion of the treadmilling F-actin network inside the protrusion (17,80,81). This flow causes friction with all structures relative to which it moves, in particular also with stress fibers and the intracellular interface of adhesion sites (75,82,83). The friction of the F-actin flow transmits the protrusion force to the substrate (22,32,75,77,82–85). The value of the friction coefficient can be perceived as the state of the clutch, with large values corresponding to an engaged state and low values to a disengaged state.

The relation between friction force and retrograde flow velocity exhibits increasing friction force at small velocities up to a critical velocity value $v_{r,cr}$, beyond which friction force decreases (Fig. 2 *A* and Eq. S19). The force maximum entails stick-slip transitions of sudden acceleration at the critical velocity due to the decrease of the force-resisting motion while the force-driving motion is maintained. Stick-slip behavior is a versatile phenomenon generating sound in bowed string instruments (86,87), causing earthquakes (88), and leading to wear in articular joints (89). Recent theoretical studies suggested it to be relevant also for protrusion dynamics (51,61,62,64,90,91) and polarization (51,62,90). Chan and Odde (92) and Wolgemuth (93) investigated the role of myosin-generated force and substrate stiffness in the clutch dynamics.

The friction force is proportional to the number of transient bonds between the F-actin network and stationary structures in the protrusion. Its biphasic character is due to fast dissociation of these bonds at fast retrograde flow (the clutch disengages) (94). They have to rebind to reach their equilibrium density after a high-velocity phase. This motivates the κ dynamics adapted from (64)

$$\frac{d\kappa_f}{dt} = c_1\left(\kappa_f^{\lim} - \left(\kappa_f - \kappa_0\right)\right) - c_2 e^{\frac{|v_{r,f}|}{c_3}}\left(\kappa_f - \kappa_0\right) + \eta_f(t), \tag{2}$$

$$\frac{d\kappa_b}{dt} = c_1\left(\kappa_b^{\lim} - \left(\kappa_b - \kappa_0\right)\right) - c_2 e^{\frac{|v_{r,b}|}{c_3}}\left(\kappa_b - \kappa_0\right) + \eta_b(t), \tag{3}$$

with an exponential acceleration of bond dissociation by retrograde flow velocity $c_2 e^{\frac{|v_{r,b}|}{c_3}}$ (94).

The maximum values $\kappa_{f,b}^{\lim}$ of $\kappa_{f,b}$ and $\zeta_{f,b}$ exhibit a Hill-type relation to the FN substrate density $B_{f,b,c}$, as specified by Eqs. S17 and S18. This

type of relation has been concluded from an earlier analysis of the adhesion-velocity relation (35). As justified in detail in the section "transitions between cell states," we assume that bond formation and breakage cause some noise on top of the deterministic dynamics, and add the noise terms $\eta_f(t)$ and $\eta_b(t)$ (see also Eq. S16). The stationary states of Eqs. 2 and 3 represent the biphasic friction force-retrograde flow velocity relation Eq. S19. The detailed equations are provided in the supporting material. The parameter values of the model are listed in Table S2.

RESULTS

Dynamic cell states

We monitored MDA-MB-231 cells migrating in FN-coated lanes over 48 h using scanning time-lapse microscopy. As described in materials and methods, rows of fields of view are sequentially imaged with 10-min or 30-s intervals per round collecting data from 144 to 16 fields of view, respectively, with on average 23 single-cell trajectories per field of view. The average single-cell trajectory length is 11.6 $\pm$ 8.0 h, limited by the fact that cells divide. We analyze in total more than 20,000 trajectories (10 min resolution) and 6000 cell trajectories (30 s resolution) (see Table S1 and Fig. S1. A representative 48-h kymograph of the 1D cell motion is depicted in Fig. 1 *A* (see also Video S1).

As described in more detail below, we observe four distinct dynamic states (Fig. 1, *B–E* and Videos S2, S3, S4, S5, and S6): a spread state with steady length (SS), a spread state with oscillatory protrusions at both ends (SO), a moving state with steady length (MS), and a moving state with an oscillating back protrusion (MO). The two moving states exist as moving up and down, so that we observe six states in total. We also exemplify six different state transitions, all of which occur on homogeneous FN lanes and without any stimulation. Therefore, we call them spontaneous transitions. The states SS and MO have also been found with RPE1 cells and NIH-3T3 fibroblasts (51), and all four dynamic states with C6 glioma cells. The oscillatory dynamics in SO and MO do not exhibit a regular period in many cases. This irregularity of repetitive protrusion events indicates a noisy excitable regime rather than regular oscillations in the strict sense of dynamical systems theory. We will see in the following section that we find regular oscillations, noisy oscillations, and a noisy excitable regime in our biophysical model.

Spread cells are symmetric and exhibit protrusions at both ends. Moving cells of course display protrusions at the front. However, we can identify additional back protrusions easily by the occurrence of negative back edge velocities in the oscillatory states, as shown by the cells in Fig. 1, *E* and *J*. Hence, moving oscillatory cells also exhibit protrusions at the front and back. We cannot tell from Fig. 1 *F* whether a protrusion exists at the back of a cell in state MS while it moves steadily. If steady protrusions at the back exist, they are most likely shorter than front protrusions (see below). However, the emergence or extension of a back protrusion precedes the direction reversal in Fig. 1 *F* by about 30 min. Hence, protrusions at front and back exist at the time of the transition, which supports the idea of direction reversals being the result of the competition of front and back protrusions, as we will see below.

Analysis of dynamic cell states

We analyze cell states on the basis of our biophysical model. Its components are explained in Fig. 2, and the equations are introduced in materials and methods and the supporting material. Eqs. 1, 2, and 3 together describe the cell dynamics in terms of cell length and the retrograde flow friction coefficient κ determined by the number of bonds between the F-actin network and structures stationary in the lab frame of reference, i.e., the clutch state.

Our model reproduces the adhesion-velocity relation in agreement with experiments (Fig. 2 *B* and section S5). This relation has been discussed in detail in Schreiber et al. (35) for cells with one protrusion in the direction of motion. The reproduction of this fundamental relation by the two-protrusion model supports our choice of modeling of the effect of FN signaling on friction and drag forces. Our model with the parameter values of Table S2 exhibits only spread states at very small FN density. The experiments show spread and moving cells in this parameter range. We use strictly symmetric protrusions with regard to parameter values in our model. Our results in Schreiber et al. (35) show excellent agreement between an asymmetric model and experimental data also at small FN densities. On that basis, we assume that protrusion asymmetry in cells causes the difference between experiments and the symmetric model at low FN density. The model predicts a stationary force-velocity relation of cell motion as shown in Fig. 2 *C*. Our results are very similar to relations predicted earlier (35,63). All predictions agree on the point that this relation reflects the retrograde flow friction law (35,63).

Analysis of cell states starts with appointing stretches of trajectories to one of the four dynamic states. The method of state classification is explained in detail in section S2.1 and Fig. S2. It analyzes cell behavior described by kymographs. Deducing states from behavior requires definition of a minimal time of consistency. If the behavior qualifies for this time as belonging to a specific state, we appoint this state to the cell. We have chosen 1 h as this time (see section S2.1). We do not classify the state of simulated cells on the basis of the known dynamic regime of the model, but rather apply the same procedure to experimental and simulated data in order to maximize compatibility of outcome.

We draw our mechanistic conclusions on the basis of the agreement between model results and experiments. The model reproduces all four dynamic states of MDA-MB-231 cells (Fig. 3 *A*). Both quantitative characteristics with regard to fraction of cells in the different states (Fig. 3 *B*) such as oscillation period, oscillation amplitude, and

velocity, and qualitative ones such as the back edge but not the front oscillating in the moving state, are met by the model (Fig. 3, *A*, *E*, and *F*).

The force-generation machinery at front and back protrusions work asymmetrically in the motile states MS and MO. This polarization between protrusions does not require any signaling to be established. It is based completely on the mechanical properties of retrograde flow. Retrograde flow is always faster at the back than at the front, since it needs to keep up with cell motion (Figs. 2 *A* and S10). Therefore, the biphasic friction force-retrograde flow velocity relation (Fig. 2 and Eq. S19) entails that the strongest coupling between F-actin network and substrate via adhesion structures forms in the front protrusion. The value of κ_f is always higher and forces are stronger in the front protrusion than in the back protrusion (Fig. 3 *E*).

Driven stick-slip systems robustly generate oscillations (86,87). A stick-slip transition of the clutch is also here the core of the oscillation mechanism of the protrusions, similar to earlier studies (51,61,62). We describe this in detail in section S4 and also explain the role of parameters. Whenever the forces driving retrograde flow drive it up to v_{cr}, the flow slips, causing the peaks in edge velocity and retrograde flow rate in Fig. 3 *E* and *F* and a sudden drop of the friction coefficient and all forces. The recovery of κ thereafter is slow and takes the larger part of the period.

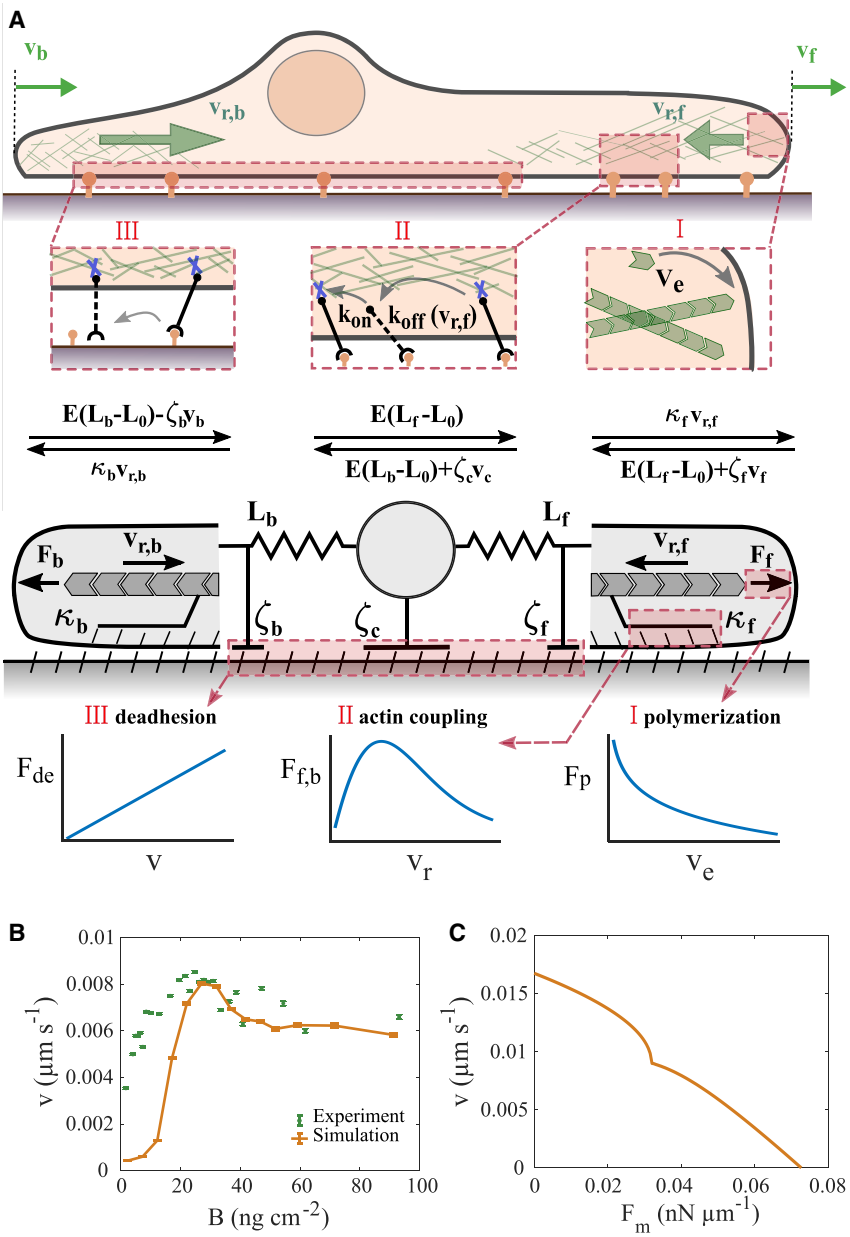

FIGURE 2 (*A*) Model constituents. Cartoon of a cell moving on a 1D fibronectin lane (*top*), force balances (*middle*), and the mechanical components of the model (*bottom*). Front and back protrusion edges move with velocities v_f and v_b, respectively. The F-actin networks flow with the retrograde flow rates $v_{r,f}$ and $v_{r,b}$, respectively. The forces $F_b = \kappa_b v_{r,b}$ and $F_f = \kappa_f v_{r,f}$ arise from polymerization of F-actin, act on the protrusion edge membrane, and drive retrograde flow against the friction forces. The front and back edge membrane experience drag with the coefficients ζ_f and ζ_b, respectively. Elastic forces $E(L_f - L_0)$ and $E(L_b - L_0)$ act between the cell body and the edges (equilibrium length L_0). The balance of the elastic forces determines the motion of the cell body against the drag force $\zeta_c v_c$. Bottom panels illustrate types of essential relations of the model. The de-attachment force of the back F_{de} is linearly related to velocity. The friction force between F-actin network retrograde flow v_r and stationary structures exhibits a maximum in its dependency on retrograde flow (clutch). The polymerization force F_p is logarithmically related to the network extension rate v_e due to the force dependency of the polymerization rate. (*B* and *C*) Two constitutive relations. (*B*) The adhesion-velocity relation. Green dots represent experimental data (see Table S1 and Data S7). Error bars represent the standard error of the mean. (*C*) The stationary force-velocity relation predicted by the model for $B = 45$ ng cm^{-2} (see section S10 for details). It provides the cell velocity under constant application of the external force F_m to the leading edge or cell body. Parameter set 1 from Table S2 is used for both panels. To see this figure in color, go online.

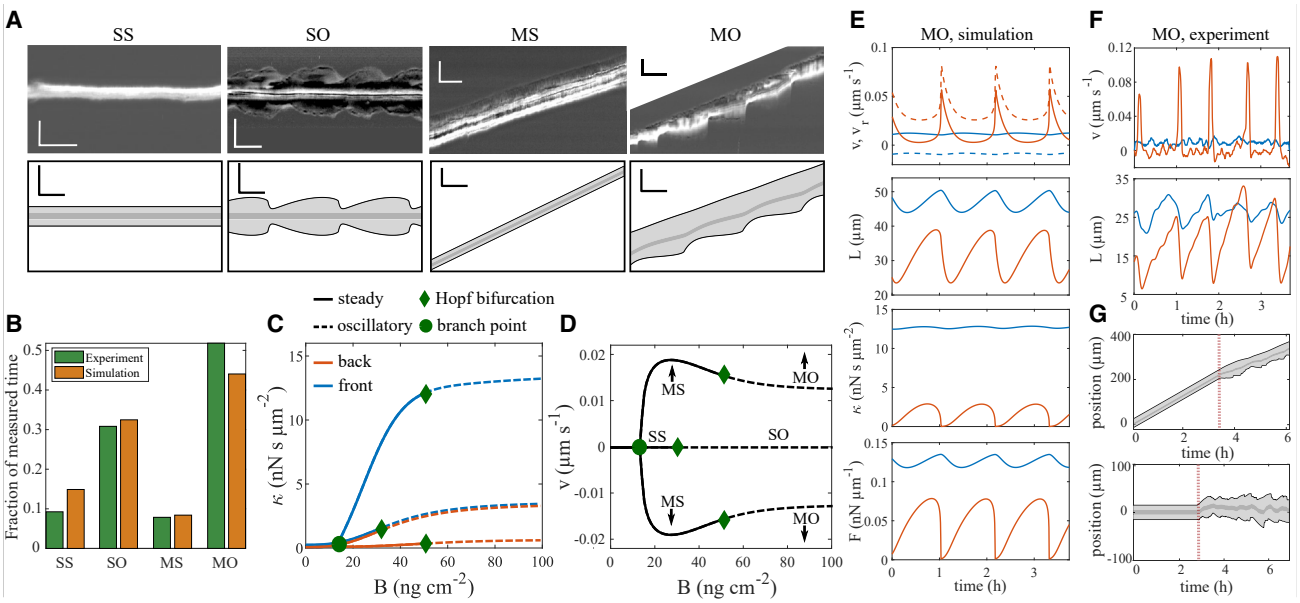

FIGURE 3 Analysis of dynamic cell states. They are either spread (SS, SO) or moving (MS, MO), and either steady (SS, MS) or oscillatory (SO, MO). (*A*) Upper panels show experiments, lower panels simulations without noise. Horizontal scale bars represent 30 min, vertical scale bars 50 μm. The cut corner of the experimental MO state showed another cell. Simulations used $c_3 = 0.0088\ \mu\text{m s}^{-1}$, SS, MS $B = 22$ ng cm^{-2}, SO $B = 36$ ng cm^{-2}, MO $B = 80$ ng cm^{-2}. (*B*) Fraction of cells in the cell states in experiment (2878 h of trajectories) and in simulations sampled from experiments on a range of fibronectin concentrations (see section S1.2 for details). (*C* and *D*) Cell states of the noise-free model illustrated by their value of the friction coefficient κ in the stationary state (*C*) and the cell velocity v (*D*) for fibronectin concentration B. Only the state SS exists at low B. At the concentration denoted as branch point, moving states appear and coexist with the spread state. Oscillations start (*dashed lines*) at the fibronectin concentrations marked as Hopf bifurcations. All moving states exist as moving up and down (*D*). (*E*) Simulation without noise of the time course of edge velocity v (*solid line*), retrograde flow v_r (*dashed line*), cell length L, friction coefficient κ, and force on the edge membrane F in state MO (*blue front*, *orange back*). (*F*) Measured time course of edge velocity and cell length in state MO (*blue front*, *orange back*). (*G*) The steady states MS (*upper panel*) and SS (*lower panel*) are excitable. They behave steadily with noise-free dynamics. Noise is switched on at the time marked by the red line. It causes behavior very similar to noisy oscillations (Fig. S5). Parameters of all simulations are listed in set 1 in Table S2.

Retrograde flow velocity v_r is equal to the network extension rate in the state SS. It is a tense state with two balanced opposing forces. This tense state is unstable against supercritical fluctuations in κ, which may arise from the concurrent snapping or formation of bonds between the F-actin network and stationary structures, and other perturbations as we will see below. The protrusion goes through one protrusion-retraction cycle upon a sufficiently strong perturbation. If these perturbations occur randomly, they are called noise. Chemical noise from random formation and breakage of bonds is omnipresent and represents relevant perturbations in systems as small as protrusions (95). The relevance of noise for adhesion and retrograde flow dynamics has been demonstrated by a variety of studies (64,90,91,96,97).

States in which small (but supercritical) perturbations may cause a large response are called excitable. Both the states SS and MS are excitable (Fig. 3 *G*). The protrusion-retraction cycle after a perturbation in the excitable regime is very similar to the oscillation cycle of noisy oscillations (Fig. S5). Therefore, the permanent noise in the bonds between the F-actin network and adhesion structures may cause oscillation-like behavior in the model cells even if they are in states SS and MS (Fig. 3 *G*). Whether the noise is supercritical—causing oscillations—or not depends on the specific parameters of the cell and the noise amplitude. Thus, the states SS and MS with low noise amplitude coexist with oscillation-like states at higher noise amplitude.

The experimental and simulated oscillations shown in Fig. 3 *A* are both rather smooth with subcritical noise, but noise may have a strong effect on state MO as we show in Fig. S5. It not only renders the time course irregular but also substantially shortens the average period. Interestingly, we find examples for both smooth (Fig. 3 *A*) and noisy oscillations (Fig. 1) in the experimental data indicating that noise amplitude is a cellular parameter and varies between individual cells. Accordingly, we have put the model noise in the clutch mechanism of retrograde flow, which is an intracellular process.

Fig. 3 *C* shows the existence of the dynamic states of the noise-free model cell in a systematic way for a range of FN coating densities. At coating densities below the value of B marked as branch point, only the spread state SS exists. Above it, spread and moving states coexist. Coexistence of several observable states for one set of parameters is multistability. At the FN density values marked as Hopf bifurcation points, oscillations start and we observe the states SO and MO. Between the branch point and the Hopf bifurcation of the spread branch, the spread state SS and moving state MS

coexist. The Hopf bifurcation of the spread state occurs at smaller FN density (B) than the one of the moving state, and thus we find a range of coexistence of SO and MS. This order of bifurcation points is swapped at other parameter values and, therefore, SS can also coexist with MO (see Fig. S5 and section S6). SO and MO coexist at large B values.

An individual cell is described in the model by a set of parameter values. The population of cells in a given experiment represents many different parameter value sets due to cell-to-cell variability. Therefore, we may find all possible pairings of coexistence in a single experiment, and both moving states can coexist with both spread states (Figs. 3 *C* and S5).

In correspondence to its versatile experimental observation, multistability of the four morphodynamic states appears to be a very robust property of mathematical models of cells on 1D lanes including the clutch. Sens (62) and Ron et al. (61) also report very similar steady and oscillatory states (but not the excitable regime) and their coexistence in noise-free models. Hennig et al. report the states SS and MO and the irregularity of oscillations in a noisy stick-slip model (51).

Transitions between cell states

All possible transitions are illustrated in Fig. 4 *A*. The fractions of transitions out of a given state are shown in Fig. 4 *B* for the experimental data. The simulations in Fig. 4 *C* show good agreement with the measurements. The same applies to the comparison of theory and experiment with latrunculin A and blebbistatin applied, shown in Fig. S7.

Transitions between the dynamic states demonstrate that an individual cell can be in different states at given fixed conditions (or at the same parameter values in modeling terms). They are the experimental manifestation of multistability. The multistability in the biophysical model is shown in Figs. 3, *C* and *D* and S5. Both spread states SS and SO can coexist with either MS or MO in the biophysical model. The upward-moving states coexist with their downward-moving analogs (Fig. 3 *C*).

Transitions between these coexisting cell states are caused by noise in the adhesion variable in the biophysical model. For several reasons we assume that noise causes also the transitions in the MDA-MB-231 cells. Cells with their typical volume in the femtoliter range are microscopic systems subject to thermal noise in many aspects of their behavior (98–101). Since adhesion sites are discrete spots, their length scales are even two orders of magnitude smaller than cell size, rendering them even more susceptible to thermal noise. Our model results show that we can reach good agreement between theory and experiment by noise in the clutch mechanism of retrograde flow. In addition, transitions occur apparently spontaneously on homogeneous FN lanes without any obvious signaling event or stimulation.

We showed above that both motile states can coexist with both spread states in the model. However, SS does not coexist with SO, and neither does MS coexist with MO in

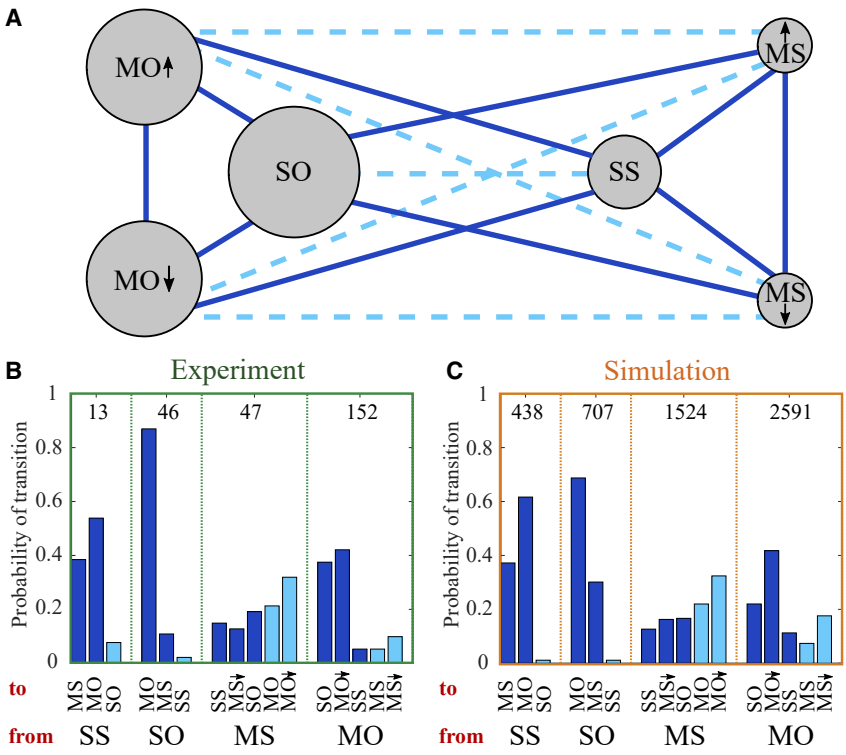

FIGURE 4 The transitions between the cell states. (*A*) The states MS moving steadily, MO moving oscillatory, SS spread steadily, and SO spread oscillatory are introduced in Fig. 3 and the text. Arrows distinguish moving up and down. The areas of circles are proportional to the fraction of cell states in experiments. Solid lines mark transitions in the sense of dynamical systems theory of multistability, i.e., between states coexisting in the noise-free mathematical model taking cell variability of parameter values of ±5% about the reference parameter set into account (see Fig. S5, section S6, and section S1.2). The state changes along dashed lines are explained in the text. (*B* and *C*) Statistics of state transitions in experiments (*B*) and simulations (*C*). The bars belonging to a specific state listed at the bottom of the panel show the fraction of transitions out of this state to one of the other states. Transition types are color-coded as in (*A*). MO↓ and MS↓ indicate direction change in the transition. Analogous results with experimental data with blebbistatin and latrunculin A applied are provided in Fig. S7. Sample size is indicated by the numbers inside the chart. Parameters of all simulations are listed in set 1 of Table S2. To see this figure in color, go online.

the bifurcation schemes in Figs. 3 *C* and S5. How, therefore, do we see transitions within these pairs of states in experimental and simulated data?

Oscillation-like protrusion events in the excitable regime occur randomly. Because of this randomness, cells may exhibit the characteristics of steady behavior for a time sufficiently long to qualify as a state and then switch to oscillation-like behavior, or vice versa. Thus, steady ↔ oscillatory transitions come out of the state analysis of the data. However, they are not state transitions in the sense of dynamical systems theory for multistable systems. Simulated and measured data behave very similar in regard to state classification and transitions, including steady ↔ oscillatory transitions. Therefore, the mechanistic ideas formulated in the model reproduce the statistics of state transitions both in the sense of multistability and the statistics of phases of consistent behavior of MDA-MB-231 cells.

The identification of steady ↔ oscillatory transitions in simulated data implies that their occurrence in experimental data does not necessarily indicate parameter value changes. Changing parameter values might be an additional reason for these transitions in experiments, since cells constantly develop and their cellular parameter values might change within the duration of an experiment of up to 48 h.

This section dealt with spontaneous state transitions. We present state transitions caused by FN steps in section S11. The biophysical model also offers an explanation for their characteristics.

Reversal of direction and the UCSP

Fig. 5 *A* shows front and back edge velocity during a direction reversal averaged over many such events including both MS and MO reversals (see Fig. S10 for the retrograde flow and Fig. S4 *E* for the network extension rate). The moment of reversal t_{rev} is the time when the cell nucleus changes direction of motion. The back edge starts to slow down about 10 min prior to t_{rev} and is already moving in the new direction (negative velocity) at the time of reversal. The front slows down after the back edge. It still moves in the old direction at t_{rev} and reverses direction only a few minutes later. Finally, it collapses in an event appearing as a negative velocity peak in Fig. 5 *A*. After the recovery of the protrusion, both edges move in the new direction with the same velocity. In agreement with this scenario, the likelihood of back protrusions increases before t_{rev} and the frequency of occurrence of front collapses after t_{rev}. Both experiments and simulations show the same scenario. A supercritical protrusion event at the back pulls sufficiently strongly to collapse the front protrusion. The back protrusion event is caused by noise in the MS state. In the MO state, protrusions occur periodically but noise generates supercritical protrusion events. We discuss forces and retrograde flow during reversal events additionally in section S9 and Figs. S5, S10, and S11.

Random direction reversals in 1D and direction changes in 2D or 3D are one reason why cells do not move permanently in their initial direction. Hence, the statistics of direction reversals and changes shape the UCSP, which we show in Fig. 5 *B* for the MDA-MB-231 cells in 1D. We find an increase of persistence time with cell velocity (in agreement with earlier results (36)). Application of latrunculin A increases persistence time. Latrunculin reduces the F-actin polymerization rate, and its application has been modeled accordingly by decreasing the force free polymerization rate V_e^0 (set 2 in Table S2). We find good agreement between experiment and simulations both for control and latrunculin A conditions, and also with blebbistatin applied (see Fig. S8).

The velocity scenario in Fig. 5 *A*, the observation that direction reversals happen only when protrusions at the front and back exist, and a strong robustness of the front protrusion against noise at the front all suggest direction reversal events to arise from competition between the front and back protrusions. As a first step in disentangling the competition mechanism, we provide a picture of protrusion stability exemplified by the state MS. The values of the two dynamic variables friction coefficient κ and protrusion length L describe the state of the model protrusions. Upon a perturbation away from its steady state, a protrusion might just go back to the steady state or collapse (Figs. 5 *C* and S9). The basin of attraction in a κ-L plot quantifies these two possibilities. If the protrusion is perturbed to a state within the basin of attraction, it relaxes back to the steady protrusion state. It collapses upon larger perturbations. Fig. 5 *C* shows that the basin of attraction of the front protrusion of fast cells is larger than the one of slow cells and vice versa for the back protrusion. Hence, the front protrusion is more stable in fast cells than in slow ones, and the back protrusion is less stable in fast cells than in slow ones.

The pulling of the back protrusion on the nucleus and the front protrusion during the direction reversal scenario described above increases the elastic force acting on the front edge membrane. This force increase speeds up retrograde flow. If the back pulls strongly enough, it drives retrograde flow velocity to the decreasing branch of the friction force-v_r relation (see Fig. 2) and shifts the state of the front protrusion from the stationary state to a trajectory outside the basin of attraction, which entails the collapse. The collapse is a rapid decrease of κ due to breaking of bonds between the F-actin network and stationary structures followed by rapid shrinkage of protrusion length due to the elastic force as shown in Fig. 5 *C* (see also the description in section S8). Remarkably, the stochastic event inside the back protrusion, which in the end causes the front protrusion collapse and direction reversal, typically occurs minutes before the moment of direction reversal.

The back pulls on the front by protruding (Fig. 5 *A*), i.e., by going through an excitation in the MS state. The slower the retrograde flow in a back protrusion, the longer the

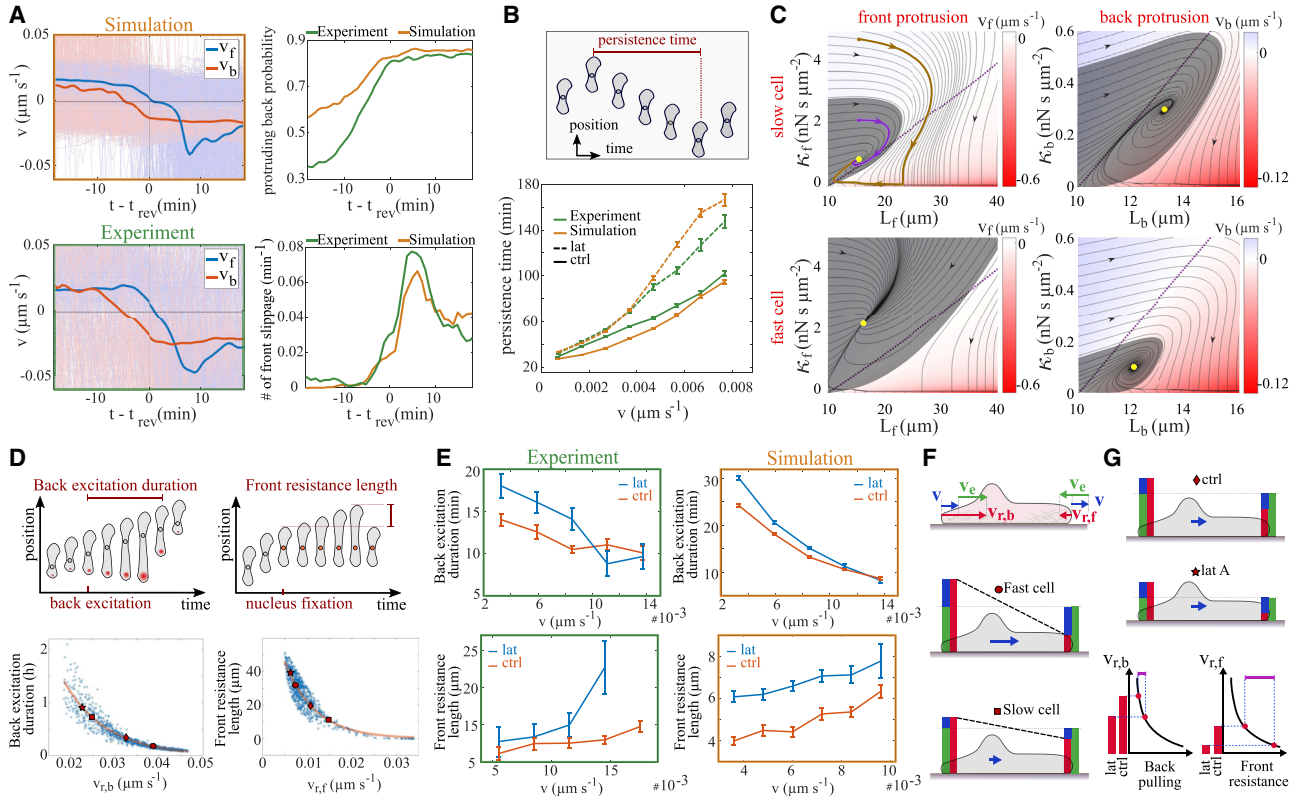

FIGURE 5 Direction reversal mechanism. (*A*) Front (v_f) and back (v_b) velocities during reversal transitions averaged over many tracks (*thin lines*, 221 experimental trajectories), including both MS and MO states. The cell nucleus changes direction at t_{rev}. For an illustrative example, see Fig. 1 *F* and the corresponding Video S6. (*B*) The relation between cell velocity and persistence time in control cells (9497 experimental trajectories) and with latrunculin A applied (3368 experimental trajectories). Latrunculin A application was modeled by decreasing the network extension rate V_e^0 from 0.030 to 0.022 μm s^{-1}. (*C*) Basin of attraction of the steady protrusion state (*gray area*) and state trajectories (*black lines*) in κ-L plots. Trajectories outside the basin of attraction (*brown*) go to small values of the friction coefficient κ and then to small protrusion length L with fast retrograde flow, which is the collapse. Trajectories starting within the basin of attraction (*purple*) lead to the steady state (*yellow dot*) without collapse. B is 20 ng cm^{-2}; velocities of fast and slow cells are 0.015 and 0.005 μm s^{-1}, respectively. (*D*) Cartoons illustrating definitions of duration of back excitation and front resistance length. Lower panels show simulations of these characteristics. Each dot marks the result of a simulation with parameter values randomly drawn from large parameter ranges (see section S1.2). (*E*) The relation between duration of back excitation and cell velocity, and front resistance length and cell velocity, in experiments and simulations (221 control experimental trajectories, 127 latrunculin A experiments). (*F*) Cartoon relations between velocities. Network extension rate (*green*) is the sum of cell velocity (*blue*) and retrograde flow velocity (*red*) in the front protrusion. Retrograde flow velocity is the sum of extension rate and cell velocity in the back protrusion, and therefore is always faster than retrograde flow in the front protrusion. (*G*) Cartoon illustrating the effect of latrunculin A. It reduces the network extension rate. Therefore, latrunculin A-treated cells have slower retrograde flow than control cells with the same cell velocity (colors as in *F*). This increases back pulling slightly and front resistance substantially (compare *D*) and thus renders the cells more persistent than control cells. Parameters of simulations in Table S2 (sets 1 and 2 for control and latrunculin conditions, respectively). Error bars represent standard error of the mean.

excitation lasts (Fig. 5 *D*). Whether it can collapse the front is determined by how long the front can resist the pulling. The slower the retrograde flow in the front protrusion, the longer it can resist. Symbols mark the retrograde flow values of typical fast and slow cells. Back excitations of fast cells are shorter, and their fronts can resist longer than slow cells. These properties of front and back protrusions hold for a large parameter range, i.e., these relations between stability characteristics and retrograde flow are fundamental and robust features.

The front resistance length is the length the front edge moves after motion arrest of the cell body. Fig. 5 *E* compares values for the duration of back excitation and front resistance length between our experimental data and simulations, and shows the qualitative agreement. Fig. 5 *F* summarizes our insights from the individual investigations. Fast cells have slow retrograde flow in the front protrusion and very fast retrograde flow in the back. This entails strong front protrusions and short excitations at the back and, hence, long persistence times. Slow cells have slower retrograde flow at the back and faster retrograde flow at the front, causing long back excitations and short front resistance length. They are therefore less persistent.

At a given velocity, latrunculin A increases persistence (Fig. 5 *B*). Application of latrunculin reduces the network extension rate and therefore reduces retrograde flow both at front and back compared with the control. This increases the duration of back excitations but even more the resistance

time and resistance length of the front, and thus renders the cell more persistent (see Fig. 5, *B* and *E* for experimental data and simulations). Fig. 5 *G* summarizes the latrunculin action graphically. We conclude that reducing network extension rate increases persistence, in agreement with our mechanistic ideas.

In summary, the protrusion competition mechanism based on elastic mechanical interaction between protrusions and cell body, nonlinear friction of retrograde flow (clutch), and noise in the clutch mechanism offers an explanation for the UCSP. The faster cells move, the slower is retrograde flow in the front protrusion, the faster is it in the back protrusion, and the more persistently the cell migrates.

DISCUSSION

We analyzed multistability of MDA-MB-231 cells on FN lanes and found in our experiments coexistence of states with oscillatory or steady cell shape, spread or moving, and moving up or down. We combined the experiments with quantitative theory, which suggests mechanistic ideas for several basic and general observations of mesenchymal motility comprising the biphasic adhesion-velocity relation, stationary force-velocity relation, UCSP, random migration, and steady, oscillatory, or excitable morphodynamics. Restricting cell motion to 1D made the relation between basic phenomena of cell motility very obvious. Random migration and the UCSP arise from random state transitions between the states "moving up" and "moving down," and the control of the parameters of the noisy clutch by integrin signaling generates the biphasic adhesion-velocity relation.

Our theory comprises three constituents, all of which are well-established experimental observations. The first one is the force balance at the protrusion edge (Eqs. S2–S4). It establishes the link between polymerization rate, cell velocity, and retrograde flow velocity (20–22,66–68). The second constituent is the noisy nonlinear friction between retrograde flow of the F-actin network and stationary structures (Eqs. S13 and S14) known as the clutch mechanism (64,75–79), which is crucial for oscillatory dynamics and multistability. Given a cell with protrusions at the front and back and symmetry with regard to parameters of the protrusions, the clutch mechanism introduces the mechanical polarization into a front protrusion with slow retrograde flow and a back protrusion with fast retrograde flow (62,90). We find that noise in the clutch mechanism due to random bonds between the F-actin network and stationary structures suffices to offer an explanation for state transitions and, thus, for the UCSP.

Multistability, oscillations, and mechanical polarization are all generated by the interaction of nonlinear F-actin flow dynamics and membrane tension without any signaling processes. Signaling sets the parameters of this system and thus determines the dynamic regime (steady, excitable, or oscillatory) and the cell velocity. A representation of the net effect of integrin signaling on drag and friction coefficients by Hill functions is the third constituent of the theory (Eqs. S17 and S18). Integrin signaling together with friction and force balance determine the adhesion-velocity relation (35). We know from Schreiber et al. (35) that a large part of cell-type-specific detail enters via this signaling constituent.

To support the idea that one mechanism explains the variety of observations, we followed the parameterization strategy to use one parameter set for all experiments with comparable conditions rather than fitting each experiment as well as possible. We were able to reach good quantitative agreement between simulations and experimental results with a single parameter set for control experiments and changes to parameter values describing drug applications corresponding to the known biochemical action of the drug. We were able to reach good agreement with regard to the types of states, the (temporal) characteristics of states, state fractions and transition probabilities, characteristics of reversal behavior, the UCSP, protrusion stability, the adhesion-velocity relation, and the behavior on FN steps. The large variety of observations agreeing between theory and experiment is a major reason for our assumption that we assembled the model constituents dominating the observed behavior, and that the mechanisms we suggest recapitulate the cellular processes. We review and discuss alternative mechanisms from literature in section S13.

Our experimental data confirm the UCSP for MDA-MB-231 cells and thus add another cell type to the many listed in Maiuri et al. (36) obeying this relation. Fast cells are more persistent than slow ones. Maiuri et al. explain the UCSP by a mechanism centered around the network extension rate: the fast network extension in fast cells advects an F-actin-binding inhibitor of network growth away from the protrusion tip and thus renders random protrusion collapse unlikely. Maiuri et al. conclude that the faster the network extension rate, the more persistently the cell moves (36). However, the data in Maiuri et al. from mature bone marrow dendritic cells migrating in a confined environment exhibiting a positive correlation between network extension rate and persistence time do not obey the UCSP (36). Furthermore, an endogenous F-actin-binding inhibitor of network extension has not been identified. Contrary to these ideas, reduction of the network extension rate by latrunculin entails an increase in persistence in our experiments and model. We found retrograde flow to be the most important indicator of stability (Fig. 5 *D*). With our approach and our data, the noisy clutch is sufficient to explain the UCSP by spontaneous direction reversals based on protrusion competition.

The mechanism suggested by Maiuri et al. implies that increasing network extension rate necessarily accompanies increasing protrusion velocity, i.e., the authors require proportionality of the velocities $v_e = av_f$ with a being constant across experimental conditions. Direct measurement of

protrusion velocity and retrograde flow in keratocytes (34) and PtK1 cells (26), and the theoretical analysis of adhesion-velocity relations for keratocytes, PtK1 cells, CHO cells, and MDA-MB-231 cells (35), come to the conclusion that this proportionality is violated. For example, increasing adhesion strength can reduce retrograde flow, entailing increasing protrusion velocity with constant or even decreasing network extension rate. Data by Jurado et al. (75) and Vicente-Manzanares et al. (12) report the relation $v_e = v_{r,f} + v_f$ (our Eq. S5), which is different from proportionality because all three velocities depend on experimental conditions (see also Fig. S4 *F*). Eq. S5 is obvious by geometrical reasoning (Fig. 2) and also compatible with a variety of measured adhesion-velocity relations (35).

The stationary force-velocity relation of cell motion represents the cell response to external force and, therefore, a basic cell property. Owing to technical problems of controlling either force or cell velocity to remain constant, it has not yet been measured, contrary to measurements and analyses of the dynamic relation, which allows both parameters to change during the experiment (20–22). Our results are very similar to relations predicted earlier (35,63). All predictions agree on the point that the stationary relation reflects the retrograde flow friction law (35,63).

CONCLUSION

We suggest as a main conclusion of our study that the basic phenomena of multistability with its dynamic regimes, adhesion-velocity relation, and UCSP can all be explained on the basis of the three model constituents force balance at the protrusion edges, noisy clutch, and integrin signaling. They also entail a specific prediction for the stationary force-velocity relation of cell motion. All three model constituents are observations which have been established earlier and in other contexts. Our study connects them and thus reveals their explanatory power. The universality of the model constituents offers a simple explanation for the universality of the constitutive relations.

DATA AVAILABILITY

Experimental data supporting the findings of this paper are available from the corresponding authors upon reasonable request. Source data of cell trajectories are provided as CSV files in the supporting material. A description of the data sets is available in section S1. Computational code is deposited on https://github.com/behnam89amiri/Multistability_and_constitutive_relations_of_cell_motion.

SUPPORTING MATERIAL

Supporting material can be found online at https://doi.org/10.1016/j.bpj.2023.02.001.

AUTHOR CONTRIBUTIONS

B.A. executed the theory and analyzed data; J.C.J.H. and C.S. executed experiments and analyzed data; M.F. designed and supervised theoretical research; J.O.R. designed and supervised experimental research; J.C.J.H., B.A., J.O.R., and M.F. wrote the paper. All authors have read and approved the published manuscript.

ACKNOWLEDGMENTS

We thank K. Rottner and T. Stradal, HZI Braunschweig, for stimulating discussions. This work was supported by the Deutsche Forschungsgemeinschaft (DFG201269156, SFB1032 to J.C.J.H., C.S., and J.O.R.).

DECLARATION OF INTERESTS

The authors declare no competing interests.

SUPPORTING CITATIONS

References (102–113) appear in the supporting material.

REFERENCES

1. Pollard, T. D., and G. G. Borisy. 2003. Cellular motility driven by assembly and disassembly of actin filaments. *Cell.* 112:453–465.
2. Abercrombie, M., J. E. Heaysman, and S. M. Pegrum. 1971. The locomotion of fibroblasts in culture: IV. Electron microscopy of the leading lamella. *Exp. Cell Res.* 67:359–367.
3. Ridley, A. J., M. A. Schwartz, …, A. R. Horwitz. 2003. Cell migration: integrating signals from front to back. *Science.* 302:1704–1709.
4. Insall, R. H., and L. M. Machesky. 2009. Actin dynamics at the leading edge: from simple machinery to complex networks. *Dev. Cell.* 17:310–322.
5. Lomakin, A. J., K. C. Lee, …, G. Danuser. 2015. Competition for actin between two distinct F-actin networks defines a bistable switch for cell polarization. *Nat. Cell Biol.* 17:1435–1445.
6. Dawes, A. T., and L. Edelstein-Keshet. 2007. Phosphoinositides and rho proteins spatially regulate actin polymerization to initiate and maintain directed movement in a one-dimensional model of a motile cell. *Biophys. J.* 92:744–768.
7. Yam, P. T., C. A. Wilson, …, J. A. Theriot. 2007. Actin–myosin network reorganization breaks symmetry at the cell rear to spontaneously initiate polarized cell motility. *J. Cell Biol.* 178:1207–1221.
8. Sheetz, M. P., D. P. Felsenfeld, and C. G. Galbraith. 1998. Cell migration: regulation of force on extracellular-matrix-integrin complexes. *Trends Cell Biol.* 8:51–54.
9. Lauffenburger, D. A., and A. F. Horwitz. 1996. Cell migration: a physically integrated molecular process. *Cell.* 84:359–369.
10. Huttenlocher, A., M. H. Ginsberg, and A. F. Horwitz. 1996. Modulation of cell migration by integrin-mediated cytoskeletal linkages and ligand-binding affinity. *J. Cell Biol.* 134:1551–1562.
11. Palecek, S. P., J. C. Loftus, …, A. F. Horwitz. 1997. Integrin-ligand binding properties govern cell migration speed through cell-substratum adhesiveness. *Nature.* 385:537–540.
12. Vicente-Manzanares, M., C. K. Choi, and A. R. Horwitz. 2009. Integrins in cell migration - the actin connection. *J. Cell Sci.* 122:199–206.
13. Parsons, J. T., A. R. Horwitz, and M. A. Schwartz. 2010. Cell adhesion: integrating cytoskeletal dynamics and cellular tension. *Nat. Rev. Mol. Cell Biol.* 11:633–643.
14. Burridge, K., and C. Guilluy. 2016. Focal adhesions, stress fibers and mechanical tension. *Exp. Cell Res.* 343:14–20.

15. Small, J. V., and J. E. Celis. 1978. Filament arrangements in negatively stained cultured cells: the organization of actin. *Cytobiologie.* 16:308–325.
16. Small, J. V., G. Isenberg, and J. E. Celis. 1978. Polarity of actin at the leading edge of cultured cells. *Nature.* 272:638–639.
17. Svitkina, T. M., A. B. Verkhovsky, …, G. G. Borisy. 1997. Analysis of the actin-myosin II system in fish epidermal keratocytes: mechanism of cell body translocation. *J. Cell Biol.* 139:397–415.
18. Small, J. V., T. Stradal, …, K. Rottner. 2002. The lamellipodium: where motility begins. *Trends Cell Biol.* 12:112–120.
19. Pollard, T. D. 2003. The cytoskeleton, cellular motility and the reductionist agenda. *Nature.* 422:741–745.
20. Prass, M., K. Jacobson, …, M. Radmacher. 2006. Direct measurement of the lamellipodial protrusive force in a migrating cell. *J. Cell Biol.* 174:767–772.
21. Heinemann, F., H. Doschke, and M. Radmacher. 2011. Keratocyte lamellipodial protrusion is characterized by a concave force-velocity relation. *Biophys. J.* 100:1420–1427.
22. Zimmermann, J., C. Brunner, …, M. Falcke. 2012. Actin filament elasticity and retrograde flow shape the force-velocity relation of motile cells. *Biophys. J.* 102:287–295.
23. Kage, F., M. Winterhoff, …, K. Rottner. 2017. FMNL formins boost lamellipodial force generation. *Nat. Commun.* 8:14832.
24. Keren, K., Z. Pincus, …, J. A. Theriot. 2008. Mechanism of shape determination in motile cells. *Nature.* 453:475–480.
25. Bretschneider, T., K. Anderson, …, G. Gerisch. 2009. The three-dimensional dynamics of actin waves, a model of cytoskeletal self-organization. *Biophys. J.* 96:2888–2900.
26. Barnhart, E. L., K.-C. Lee, …, J. A. Theriot. 2011. An adhesion-dependent switch between mechanisms that determine motile cell shape. *PLoS Biol.* 9:e1001059.
27. Schaub, S., S. Bohnet, V. M. Laurent, J.-J. Meister, and A. B. Verkhovsky. 2007. Comparative maps of motion and assembly of filamentous actin and myosin II in migrating cells. *Mol. Biol. Cell.* 18:3723–3732.
28. Shao, D., H. Levine, and W.-J. Rappel. 2012. Coupling actin flow, adhesion, and morphology in a computational cell motility model. *Proc. Natl. Acad. Sci. USA.* 109:6851–6856.
29. Ziebert, F., and I. S. Aranson. 2013. Effects of adhesion dynamics and substrate compliance on the shape and motility of crawling cells. *PLoS One.* 8:e64511.
30. DiMilla, P. A., K. Barbee, and D. A. Lauffenburger. 1991. Mathematical model for the effects of adhesion and mechanics on cell migration speed. *Biophys. J.* 60:15–37.
31. DiMilla, P. A., J. A. Stone, …, D. A. Lauffenburger. 1993. Maximal migration of human smooth muscle cells on fibronectin and type IV collagen occurs at an intermediate attachment strength. *J. Cell Biol.* 122:729–737.
32. Munevar, S., Y. Wang, and M. Dembo. 2001. Traction force microscopy of migrating normal and H-ras transformed 3T3 fibroblasts. *Biophys. J.* 80:1744–1757.
33. Mueller, J., G. Szep, …, M. Sixt. 2017. Load adaptation of lamellipodial actin networks. *Cell.* 171:188–200.e16.
34. Gupton, S. L., and C. M. Waterman-Storer. 2006. Spatiotemporal feedback between actomyosin and focal-adhesion systems optimizes rapid cell migration. *Cell.* 125:1361–1374.
35. Schreiber, C., B. Amiri, …, M. Falcke. 2021. On the adhesion–velocity relation and length adaptation of motile cells on stepped fibronectin lanes. *Proc. Nat. Acad. Sci. USA.* 118:e2009959118.
36. Maiuri, P., J.-F. Rupprecht, …, R. Voituriez. 2015. Actin flows mediate a universal coupling between cell speed and cell persistence. *Cell.* 161:374–386.
37. Giannone, G., B. J. Dubin-Thaler, …, M. P. Sheetz. 2004. Periodic lamellipodial contractions correlate with rearward actin waves. *Cell.* 116:431–443.
38. Döbereiner, H. G., B. J. Dubin-Thaler, …, M. P. Sheetz. 2006. Lateral membrane waves constitute a universal dynamic pattern of motile cells. *Phys. Rev. Lett.* 97:038102.
39. Gholami, A., M. Falcke, and E. Frey. 2008. Velocity oscillations in actin-based motility. *New J. Phys.* 10:033022.
40. Enculescu, M., A. Gholami, and M. Falcke. 2008. Dynamic regimes and bifurcations in a model of actin-based motility. *Phys. Rev. E - Stat. Nonlinear Soft Matter Phys.* 78:031915.
41. Enculescu, M., M. Sabouri-Ghomi, …, M. Falcke. 2010. Modeling of protrusion phenotypes driven by the actin-membrane interaction. *Biophys. J.* 98:1571–1581.
42. Allard, J., and A. Mogilner. 2013. Traveling waves in actin dynamics and cell motility. *Curr. Opin. Cell Biol.* 25:107–115.
43. Koestler, S. A., S. Auinger, …, J. V. Small. 2008. Differentially oriented populations of actin filaments generated in lamellipodia collaborate in pushing and pausing at the cell front. *Nat. Cell Biol.* 10:306–313.
44. Burnette, D. T., S. Manley, …, J. Lippincott-Schwartz. 2011. A role for actin arcs in the leading-edge advance of migrating cells. *Nat. Cell Biol.* 13:371–381.
45. Zimmermann, J., and M. Falcke. 2014. formation of transient lamellipodia. *PLoS One.* 9:e87638.
46. Barnhart, E. L., J. Allard, …, A. Mogilner. 2017. Adhesion-dependent wave generation in crawling cells. *Curr. Biol.* 27:27–38.
47. Bolado-Carrancio, A., O. S. Rukhlenko, …, B. N. Kholodenko. 2020. Periodic propagating waves coordinate RhoGTPase network dynamics at the leading and trailing edges during cell migration. *Elife.* 9:e58165.
48. Doubrovinski, K., and K. Kruse. 2011. Cell motility resulting from spontaneous polymerization waves. *Phys. Rev. Lett.* 107:258103.
49. Beta, C., and K. Kruse. 2017. Intracellular oscillations and waves. *Annu. Rev. Condens. Matter Phys.* 8:239–264.
50. Gerhardt, M., M. Ecke, …, G. Gerisch. 2014. Actin and PIP3 waves in giant cells reveal the inherent length scale of an excited state. *J. Cell Sci.* 127:4507–4517.
51. Hennig, K., I. Wang, …, M. Balland. 2020. Stick-slip dynamics of cell adhesion triggers spontaneous symmetry breaking and directional migration of mesenchymal cells on one-dimensional lines. *Science Advances.* 6:eaau5670.
52. Park, J., W. R. Holmes, …, A. Levchenko. 2017. Mechanochemical feedback underlies coexistence of qualitatively distinct cell polarity patterns within diverse cell populations. *Proc. Natl. Acad. Sci. USA.* 114:E5750–E5759.
53. Lee, S. H., J. C. Hou, …, A. Levchenko. 2022. A molecular clock controls periodically driven cell migration in confined spaces. *Cell Syst.* 13:514–529.e10.
54. Verkhovsky, A. B., T. M. Svitkina, and G. G. Borisy. 1999. Self-polarization and directional motility of cytoplasm. *Curr. Biol.* 9:11–20.
55. Hawkins, R. J., R. Poincloux, …, R. Voituriez. 2011. Spontaneous contractility-mediated cortical flow generates cell migration in three-dimensional environments. *Biophys. J.* 101:1041–1045.
56. Ziebert, F., S. Swaminathan, and I. S. Aranson. 2012. Model for self-polarization and motility of keratocyte fragments. *J. R. Soc. Interface.* 9:1084–1092.
57. Tjhung, E., D. Marenduzzo, and M. E. Cates. 2012. Spontaneous symmetry breaking in active droplets provides a generic route to motility. *Proc. Natl. Acad. Sci. USA.* 109:12381–12386.
58. Ruprecht, V., S. Wieser, …, C. P. Heisenberg. 2015. Cortical contractility triggers a stochastic switch to fast amoeboid cell motility. *Cell.* 160:673–685.
59. Kozlov, M. M., and A. Mogilner. 2007. Model of polarization and bistability of cell fragments. *Biophys. J.* 93:3811–3819.
60. Holmes, W. R., J. Park, …, L. Edelstein-Keshet. 2017. A mathematical model coupling polarity signaling to cell adhesion explains

diverse cell migration patterns. *PLoS Comput. Biol.* 13:10055244–e1005622.

61. Ron, J. E., P. Monzo, …, N. S. Gov. 2020. One-dimensional cell motility patterns. *Phys. Rev. Research.* 2:033237.
62. Sens, P. 2020. Stick–slip model for actin-driven cell protrusions, cell polarization, and crawling. *Proc. Natl. Acad. Sci. USA.* 117:24670–24678.
63. Zimmermann, J., M. Enculescu, and M. Falcke. 2010. Leading edge - gel coupling in lamellipodium motion. *Phys. Rev. E - Stat. Nonlinear Soft Matter Phys.* 82:051925.
64. Craig, E. M., J. Stricker, …, A. Mogilner. 2015. Model for adhesion clutch explains biphasic relationship between actin flow and traction at the cell leading edge. *Phys. Biol.* 12:035002.
65. Schreiber, C., F. J. Segerer, …, J. O. Rädler. 2016. Ring-shaped microlanes and chemical barriers as a platform for probing single-cell migration. *Sci. Rep.* 6:26858.
66. Mogilner, A., and G. Oster. 2003. Force generation by actin polymerization II: the elastic ratchet and tethered filaments. *Biophys. J.* 84:1591–1605.
67. Footer, M. J., J. W. J. Kerssemakers, …, M. Dogterom. 2007. Direct measurement of force generation by actin filament polymerization using an optical trap. *Proc. Natl. Acad. Sci. USA.* 104:2181–2186.
68. Gholami, A., J. Wilhelm, and E. Frey. 2006. Entropic forces generated by grafted semiflexible polymers. *Phys. Rev. E - Stat. Nonlinear Soft Matter Phys.* 74:041803.
69. Wilson, K., A. Lewalle, …, G. Charras. 2013. Mechanisms of leading edge protrusion in interstitial migration. *Nat. Commun.* 4:2896.
70. Guo, M., A. F. Pegoraro, …, D. A. Weitz. 2017. Cell volume change through water efflux impacts cell stiffness and stem cell fate. *Proc. Natl. Acad. Sci. USA.* 114:E8618–E8627.
71. Motahari, F., and A. E. Carlsson. 2019. Thermodynamically consistent treatment of the growth of a biopolymer in the presence of a smooth obstacle interaction potential. *Phys. Rev. E.* 100:042409.
72. Mitchison, T., and M. Kirschner. 1988. Cytoskeletal dynamics and nerve growth. *Neuron.* 1:761–772.
73. Suter, D. M., and P. Forscher. 1998. An emerging link between cytoskeletal dynamics and cell adhesion molecules in growth cone guidance. *Curr. Opin. Neurobiol.* 8:106–116.
74. Suter, D. M., and P. Forscher. 2000. Substrate–cytoskeletal coupling as a mechanism for the regulation of growth cone motility and guidance. *J. Neurobiol.* 44:97–113.
75. Jurado, C., J. R. Haserick, and J. Lee. 2005. Slipping or gripping? Fluorescent speckle microscopy in fish keratocytes reveals two different mechanisms for generating a retrograde flow of actin. *Mol. Biol. Cell.* 16:507–518.
76. Hu, K., L. Ji, …, C. M. Waterman-Storer. 2007. Differential transmission of actin motion within focal adhesions. *Science.* 315:111–115.
77. Gardel, M. L., B. Sabass, …, C. M. Waterman. 2008. Traction stress in focal adhesions correlates biphasically with actin retrograde flow speed. *J. Cell Biol.* 183:999–1005.
78. Aratyn-Schaus, Y., and M. L. Gardel. 2010. Transient frictional slip between integrin and the ECM in focal adhesions under myosin II tension. *Curr. Biol.* 20:1145–1153.
79. Li, Y., P. Bhimalapuram, and A. R. Dinner. 2010. Model for how retrograde actin flow regulates adhesion traction stresses. *J. Phys. Condens. Matter.* 22:194113.
80. Heath, J. P., and B. F. Holifield. 1993. On the mechanisms of cortical actin flow and its role in cytoskeletal organisation of fibroblasts. *Symp. Soc. Exp. Biol.* 47:35–56.
81. Vallotton, P., G. Danuser, …, A. B. Verkhovsky. 2005. Tracking retrograde flow in keratocytes: news from the front. *Mol. Biol. Cell.* 16:1223–1231.
82. Renkawitz, J., K. Schumann, …, M. Sixt. 2009. Adaptive force transmission in amoeboid cell migration. *Nat. Cell Biol.* 11:1438–1443.
83. Alexandrova, A. Y., K. Arnold, …, A. B. Verkhovsky. 2008. Comparative dynamics of retrograde actin flow and focal adhesions: formation of nascent adhesions triggers transition from fast to slow flow. *PLoS One.* 3:e3234.
84. Choquet, D., D. P. Felsenfeld, and M. P. Sheetz. 1997. Extracellular matrix rigidity causes strengthening of integrin–cytoskeleton linkages. *Cell.* 88:39–48.
85. Fournier, M. F., R. Sauser, …, A. B. Verkhovsky. 2010. Force transmission in migrating cells. *J. Cell Biol.* 188:287–297.
86. Ebeling, W. 1989. Chaos, Ordnung und Information. Urania Verlag Leipzig.
87. Popp, K., and P. Stelter. 1990. Stick-slip vibrations and chaos. *Phil. Trans. Phys. Sci. Eng.* 332:89–105.
88. Brace, W. F., and J. D. Byerlee. 1966. Stick-slip as a mechanism for earthquakes. *Science.* 153:990–992.
89. Lee, D. W., X. Banquy, and J. N. Israelachvili. 2013. Stick-slip friction and wear of articular joints. *Proc. Natl. Acad. Sci. USA.* 110:E567–E574.
90. Barnhart, E., K.-C. Lee, …, A. Mogilner. 2015. Balance between cell-substrate adhesion and myosin contraction determines the frequency of motility initiation in fish keratocytes. *Proc. Natl. Acad. Sci. USA.* 112:5045–5050.
91. Rutkowski, D. M., and D. Vavylonis. 2021. Discrete mechanical model of lamellipodial actin network implements molecular clutch mechanism and generates arcs and microspikes. *PLoS Comput. Biol.* 17:e1009506–e1009532.
92. Chan, C. E., and D. J. Odde. 2008. Traction dynamics of Filopodia on compliant substrates. *Science.* 322:1687–1691.
93. Wolgemuth, C. W. 2005. Lamellipodial contractions during crawling and spreading. *Biophys. J.* 89:1643–1649.
94. Evans, E. 2001. Probing the relation between force - lifetime - and chemistry in single molecular bonds. *Annu. Rev. Biophys. Biomol. Struct.* 30:105–128.
95. van Kampen, N. 2001. Stochastic Processes in Physics and Chemistry. North-Holland, Amsterdam.
96. Cirit, M., M. Krajcovic, …, J. M. Haugh. 2010. Stochastic model of integrin-mediated signaling and adhesion dynamics at the leading edges of migrating cells. *PLoS Comput. Biol.* 6:e1000688.
97. Weichsel, J., and U. S. Schwarz. 2010. Two competing orientation patterns explain experimentally observed anomalies in growing actin networks. *Proc. Natl. Acad. Sci. USA.* 107:6304–6309.
98. Bhalla, U. S. 2004. Signaling in small subcellular volumes. I. Stochastic and diffusion effects on individual pathways. *Biophys. J.* 87:733–744.
99. Bialek, W., and S. Setayeshgar. 2005. Physical limits to biochemical signaling. *Proc. Natl. Acad. Sci. USA.* 102:10040–10045.
100. Tsimring, L. S. 2014. Noise in biology. *Rep. Prog. Phys.* 77:026601.
101. Falcke, M. 2017. Life is change – dynamic modeling quantifies it. *Curr. Opin. Struct. Biol.* 3:iv–viii.
102. Coué, M., S. L. Brenner, …, E. D. Korn. 1987. Inhibition of actin polymerization by latrunculin A. *FEBS Lett.* 213:316–318.
103. McGrath, J. L., N. J. Eungdamrong, …, S. C. Kuo. 2003. The force-velocity relationship for the actin-based motility of Listeria monocytogenes. *Curr. Biol.* 13:329–332.
104. Koseki, K., D. Taniguchi, …, N. Watanabe. 2019. Lamellipodium tip actin barbed ends serve as a force sensor. *Gene Cell.* 24:705–718.
105. Peskin, C. S., G. M. Odell, and G. F. Oster. 1993. Cellular motions and thermal fluctuations: the Brownian ratchet. *Biophys. J.* 65:316–324.
106. Bieling, P., T. D. Li, …, R. D. Mullins. 2016. Force feedback controls motor activity and mechanical properties of self-assembling branched actin networks. *Cell.* 164:115–127.
107. Dolati, S., F. Kage, …, M. Falcke. 2018. On the relation between filament density, force generation, and protrusion rate in mesenchymal cell motility. *Mol. Biol. Cell.* 29:2674–2686.

108. Dickinson, R. B., and D. L. Purich. 2002. Clamped-filament elongation model for actin-based motors. *Biophys. J.* 82:605–617.

109. Trichet, L., O. Campàs, …, J. Plastino. 2007. VASP governs actin dynamics by modulating filament anchoring. *Biophys. J.* 92:1081–1089.

110. d'Alessandro, J., A. Barbier-Chebbah, …, B. Ladoux. 2021. Cell migration guided by long-lived spatial memory. *Nat. Commun.* 12:4118.

111. Harburger, D. S., and D. A. Calderwood. 2009. Integrin signalling at a glance. *J. Cell Sci.* 122:159–163.

112. Warner, H., B. J. Wilson, and P. T. Caswell. 2019. Control of adhesion and protrusion in cell migration by Rho GTPases. *Curr. Opin. Cell Biol.* 56:64–70.

113. Tkachenko, E., M. Sabouri-Ghomi, …, M. H. Ginsberg. 2011. Protein kinase A governs a RhoA-RhoGDI protrusion-retraction pacemaker in migrating cells. *Nat. Cell Biol.* 13:660–667.

Biophysical Journal, Volume *122*

Supplemental information

On multistability and constitutive relations of cell motion on fibronectin lanes

Behnam Amiri, Johannes C.J. Heyn, Christoph Schreiber, Joachim O. Rädler, and Martin Falcke

Biophysical*Journal*
Supporting Material

On multistability and constitutive relations of cell motion on Fibronectin lanes

Behnam Amiri[1], Johannes C.J. Heyn[2], Christoph Schreiber[2], Joachim O. Rädler[2,*], and Martin Falcke[1,3,*]

[1]Max Delbrück Center for Molecular Medicine in the Helmholtz Association, Robert Rössle Str. 10, 13125 Berlin, Germany
[2]Fakultät für Physik, Ludwig-Maximilians-Universität München (LMU), Geschwister-Scholl-Platz 1, 80539 Munich, Germany
[3]Dept. of Physics, Humboldt University, Newtonstr. 15, 12489 Berlin, Germany
[*]Correspondence: martin.falcke@mdc-berlin.de or raedler@lmu.de

S1 DATA SETS AND SIMULATIONS

S1.1 Data sets

Experimental data was recorded in two different temporal resolutions, 30 s and 10 min, respectively. Data with high temporal resolution allows the study of the dynamics of the cell edges. But the number of cell tracks per experiment is limited by the fact that only a limited number of field of views can be covered during a time step of 30 s. The lower temporal resolution of 10 min enabled the acquisition of much bigger data sets which in turn facilitate the study of characteristics such as persistence time as defined below. In the data sets with 10 min temporal resolution, about 22900 single-cell tracks that are moving on homogeneous Fibronectin lanes with densities in the range of 0-120 ng cm^{-2} were analysed. The data sets with 30 s temporal resolution comprise of about 400 single-cell tracks (about 6400 h) on homogeneous Fibronectin lanes with densities in the range of 0-40 ng cm^{-2}. Data sets 1-3 consist of data from 4 independent experiments acquired with 30 s temporal resolution and data sets 4-7 of data from 6 independent experiments with a temporal resolution of 10 min.

For high temporal resolution data sets 1-3 the first column contains the cell track ID, the second the time in the lab frame (s), the third the position of the centre of nucleus along the FN lane (μm), the fourth the median FN density along the FN lane of the cell (ng cm^{-2}), the fifth the position of the cell's upper edge along the lane (μm), the sixth the position of the cell's lower edge (μm), the seventh the position of the nucleus' upper edge, the eighth the position of the nucleus' lower edge, and the ninth the state change points. For the simulation data sets the tenth and eleventh columns contain the retrograde flow velocity at the upper and lower protrusions respectively, and the twelfth column contains the critical retrograde velocity of each cell. For low temporal resolution data sets 4-7 the first column contains the cell track ID, the second the time in the lab frame (min), the third the position of the nucleus along the FN lane (μm) and the fourth the median FN density along the FN lane of the cell (ng cm^{-2}). Data for cell trajectories on stepped FN lanes is taken from (1). This data set comprises of about 6200 single-cell tracks. For a list of all experimental data sets, see Table S1.

Name of data set	Temporal resolution	Treatment	Number of cell tracks	Total trajectory time	Figures
1_ctrl_30s	30 s	control	221	2878 h	1,3-5
2_lat_30s	30 s	Latrunculin A	127	2343 h	5, S7
3_blebb_30s	30 s	Blebbistatin	65	1165 h	S7
4_ctrl_10min	10 min	control	9497	96577 h	5
5_lat_10min	10 min	Latrunculin A	3368	54809 h	5
6_blebb_10min	10 min	Blebbistatin	3728	47638 h	S8
7_untreated_10min	10 min	untreated	6261	65378 h	2
stepped lanes	10 min	untreated	6158	76759 h	S14

Table S1: List of data sets containing experimental cell trajectories.

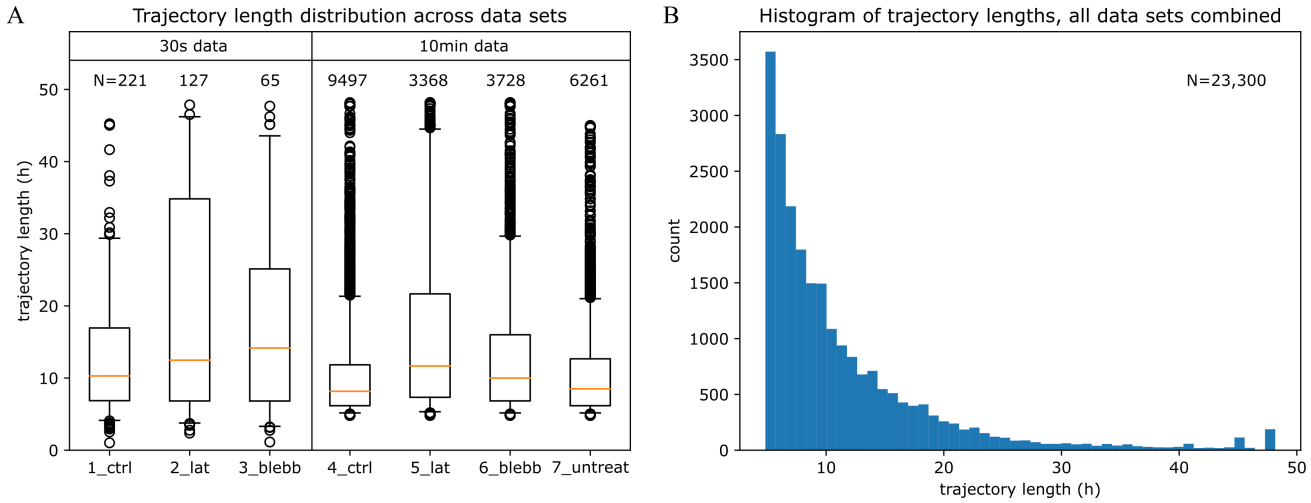

Figure S1: **Distribution of lengths of cell trajectories.** (A) Boxplots of data sets 1-7, see Table S1. Orange lines mark the median track length and the box edges the first and third quartile, respectively. The whiskers indicate the 5%- and 95%-percentile. N indicates the number of cell trajectories. The average trajectory length across all data sets is 11.6 h. With a median trajectory length of 8.8 h the distribution is right-skewed meaning that the number of trajectories shorter than the average is much greater than of those being longer. The maximum length is 48 h due to the set duration of the experiments. (B) Histogram of trajectory lengths for all data sets combined. The aforementioned skewness is apparent, with counts decreasing for longer trajectory lengths.

S1.2 Simulations

All simulations were performed in MATLAB (Mathworks). We have 2 experimental control data sets (set 1 and the step experiments set 4 in Table S2) with the experiments done in different months. Set 1 comprises experiments on homogeneous lanes and has been used for the data in Figs. 3, 4 and 5. Set 4 are the experiments on stepped Fibronectin lanes in Fig. S14. Parameter values obtained from the fits vary slightly between the two sets most likely due to day-to-day variability of cell behaviour (Table S2).

From a modelling point of view, drug treatment appears in the model as parameter change resulting from fits to experimental data with the corresponding drug applied. Latrunculin reduces the actin polymerisation rate (2). Very much in agreement with this known action of Latrunculin, a reduction of the polymerisation rate V_e^0 from 0.03 μms^{-1} in set 1 control simulations to 0.022 μms^{-1} in set 2 Latrunculin simulations was sufficient to fit the Latrunculin data in Fig. 5.

The myosin inhibition upon Blebbistatin application affects the integrin signaling pathway, which is manifested by the variation of κ and ζ. In an earlier study on the adhesion-velocity relation fitting data of 4 different cell types with very good agreement to a model with one protrusion only, we also allowed for contractile action of myosin (1). It turned out to be negligible in all 4 cell types including MDA-MB-231 cells. Also now, changes in the values of the parameters κ^{max} and ζ^{max} were sufficient to simulate the effect of Blebbistatin treatment (set 3 in Table S2). Our finding here, that the action of Blebbistatin can be fit by modifying the representation of the integrin signalling pathway only, very much confirms the earlier results, and is in agreement with results reported by Hennig et al. (3) for RPE1 cells and NIH-3T3 fibroblasts. Hence, we find the effect of myosin as part of the integrin signalling pathway to be more relevant than as contractile driver of retrograde flow in MDA-MB-231 cells.

We simulated a total number of approximately 6100 cell tracks with a length of 15 hours each. That includes 2500 cell tracks for the control condition, 2800 cell tracks for the Latrunculin condition, and 800 cell tracks for the Blebbistatin condition. Simulations start with a randomly chosen initial state of the cell. The Fibronectin densities on lanes are homogeneous in simulation sets 1, 2, and 3. Cell tracks in each experimental data set comprise a range of Fibronectin densities. We used the same values of Fibronectin densities in the simulations. All analyses in Figs. 3-5 are carried out by averaging over the Fibronectin density values with an ensemble of simulations with the same weight of the Fibronectin densities as in the experiments.

In case of the simulations for the experiments on stepped lanes, we reproduced the exact densities on the individual steps of the individual lanes and averaged within the ensemble of simulations with the same rules as on homogeneous lanes. For the stepped lanes we simulated a total number of approximately 1200 cell tracks.

Cell to cell variability is an important factor in the experiments affecting the population's behaviour. Therefore, we included the cell variability in the simulations by parameter variability. The model parameters in each simulation set are chosen according

Parameter	**Set 1: control**	**Set 2: Latrunculin**	**Set 3: Blebbistatin**	**Set 4: stepped lanes**	**Units**
Figures	Figs. 2, 3, 4, 5, S4, S5, S6, S9, S10, S11, S12	Figs. 5, S7	Figs. S7, S8	Figs. S13, S14	
E	3e−3	3e−3	3e−3	3e−3	$\mathrm{nN\mu m^{-2}}$
L_0	10	10	10	10	μm
V_e^0	3e−2	2.2e−2	3e−2	3e−2	$\mu\mathrm{ms^{-1}}$
k^-	5e−3	5e−3	5e−3	3e−3	$\mu\mathrm{ms^{-1}}$
c_1	1.5e−4	1.5e−4	1.5e−4	2e−4	$\mathrm{s^{-1}}$
c_2	7.5e−5	7.5e−5	7.5e−5	1e−4	$\mathrm{s^{-1}}$
c_3	7.8e−3	7.8e−3	7.8e−3	8e−3	$\mu\mathrm{ms^{-1}}$
κ^{max}	35	35	20	30	$\mathrm{nNs\mu m^{-2}}$
K_κ	35	35	35	20	$\mathrm{ngcm^{-2}}$
n_κ	3	3	3	3	
κ_0	1e−2	1e−2	1e−2	1e−1	$\mathrm{nNs\mu m^{-2}}$
ζ^{max}	1.4	1.4	1.2	2.4	$\mathrm{nNs\mu m^{-2}}$
K_ζ	50	50	50	50	$\mathrm{ngcm^{-2}}$
n_ζ	4	4	4	4	
b	3	3	3	2	
ζ_0	1e−1	1e−1	1e−1	2e−1	$\mathrm{nNs\mu m^{-2}}$
α	4e−2	4e−2	4e−2	4e−2	$\mathrm{nN^{-2}s^{-2}\mu m^4}$

Table S2: Parameters used for simulations. Parameter set 1 is used for simulations in control condition, set 2 for Latrunculin, and set 3 for Blebbistatin conditions. Simulations with sets 1, 2, and 3 are all carried out on homogeneous Fibronectin lanes. Parameter set 4 is used in the simulations on stepped Fibronectin lanes.

to Table S2, with an allowed variability of ±5% to mimic cell variability in experiments.

The simulations in Fig. 5D were performed with an allowed variability of ±50%. For simplicity of the analysis, we only consider the cell tracks that are in the MS state when the noise is switched off. In the back excitation simulations (left panels in Fig. 5D), cells move (MS state) for 3 h without noise in the system. Then we apply noise to the back protrusion (Eq. S14). A back excitation is defined as a peak of cell length with at least 3 μmamplitude. The back excitation duration for each cell track is determined by averaging the duration of all back excitation events. The back retrograde flow for each cell track is calculated from the noise-free steady state.

In the front resistance simulations (right panels in Fig. 5D), noise is switched off throughout the simulations. We arrest the cell body motion instantaneously after 3 h of steady state motion. The front edge continues to move, which stretches the front protrusion. The front resistance length is defined as the difference between the maximum cell length before collapsing and the noise-free steady state cell length. The front retrograde flow for each cell track is calculated from the noise-free steady state before the nucleus fixing.

S2 DATA ANALYSIS

We used the kymographs of single-cell tracks to analyse the cell states. To exclude the interactions of cells, we terminated a single-cell kymograph when it got too close to a neighbouring cell. Then we found the position of the cell edges by segmenting manually the kymographs in FIJI (ImageJ) using a self-made macro. The same manual segmentation process was used for the nucleus, resulting in the data of the position of the nucleus edges (Fig. S2A).

S2.1 Classification of cell states

Our classification method described below analyses cell behaviour obtained from kymographs. We used stretches of trajectories excluding interactions between cells which entails stretches shorter than the duration of the experiment. Deducing states from behaviour requires the definition of a minimal time of consistency t_c. If the behaviour during this time qualifies as belonging to a specific state, we appoint this state to the cell. We chose 1h as this time, which is sufficiently larger than typical oscillation periods of about 15 min. and allowed to distinguish steady and oscillatory states. Detection of transitions requires stretches of

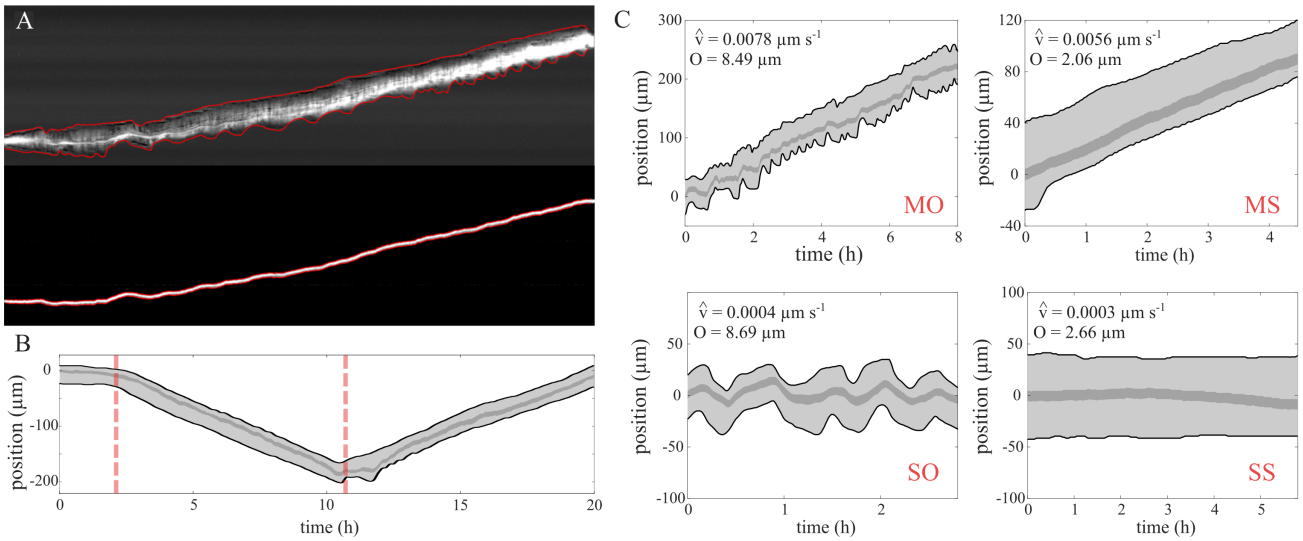

Figure S2: **Classification of cell states.** (A) Manual segmentation of the cell (upper panel) and nucleus kymographs (lower panel). The red lines show the segmented outlines of the kymographs. (B) State change points of a cell track. The dashed red lines indicate the time frames of a state change of the cell. (C) Examples of identified states. The values of the average velocity $\hat{v}$ and oscillation metric O shown in each panel determine the state of the cell. All the kymographs are from experiments.

tracks of at least $2t_c$ in order to identify the state before the transition and the state after it as different. Since transitions happen rarely just in the middle of a trajectory, stretches of several times $2t_c$ are required for state transition analysis. That requirement limits the length of t_c from above.

S2.1.1 State change points

We split the single-cell tracks into different states. For this reason, a method is employed which uses an iterative change-point analysis based on cumulative sum (CUSUM) statistics similar to (4) to find the transition points between the two states of a cell. This algorithm is able to detect the time points with a fundamental change of motility trend. The period between two subsequent change points is defined as an episode of the cell with a specific state. Any episode lasting shorter than 1 h is disregarded and appended to the preceding episode. The detected state change points are shown in Fig. S2B for a cell track.

S2.1.2 State identification

We employed two criteria to determine the closest match to the states SS, SO, MS, and MO during an episode of the cell. First, to assess whether the cell is moving or spread, we compare the average velocity of the cell during the episode with a critical speed (0.002 µms^{-1}). Cells with an average velocity smaller than this critical speed are considered spread.

The many cases of out-of-phase relations of the observed oscillations entail not only length dynamics but also motion of the nucleus. It turned out, that we get the most reliable classification when including both the length dynamics and the nuclear position dynamics. In the first step, we remove the small fluctuations of the length and cell body position. These fluctuations do not represent the oscillations caused by the mechanisms discussed in this study. Similarly, prolonged slow length changes are also not caused by the oscillation. They can be attributed to very slow cell processes that change cell properties like membrane tension and elasticity on long time scales. Long-term trends of cell body position are also related to the general motion of the cell rather than nucleus movements due to the cell oscillations. So, we apply a band-pass filter to the length and cell body position data to remove the tiny fluctuations and long trends. We chose the cutoff frequencies of 1 and 6 h^{-1} to remove the variations with time scales shorter than 10 min and longer than 1 h.

This filtered data contains the variations of length and cell body position in the time scales relevant to the oscillations caused by the competition of protrusions. For an oscillatory state, filtered length and/or cell body position vary a lot, while they stay almost constant in time for a steady state. Thus, the summation of the average absolute deviation of the filtered length and the average absolute deviation of the filtered cell body position is an indicator of the degree of oscillations.

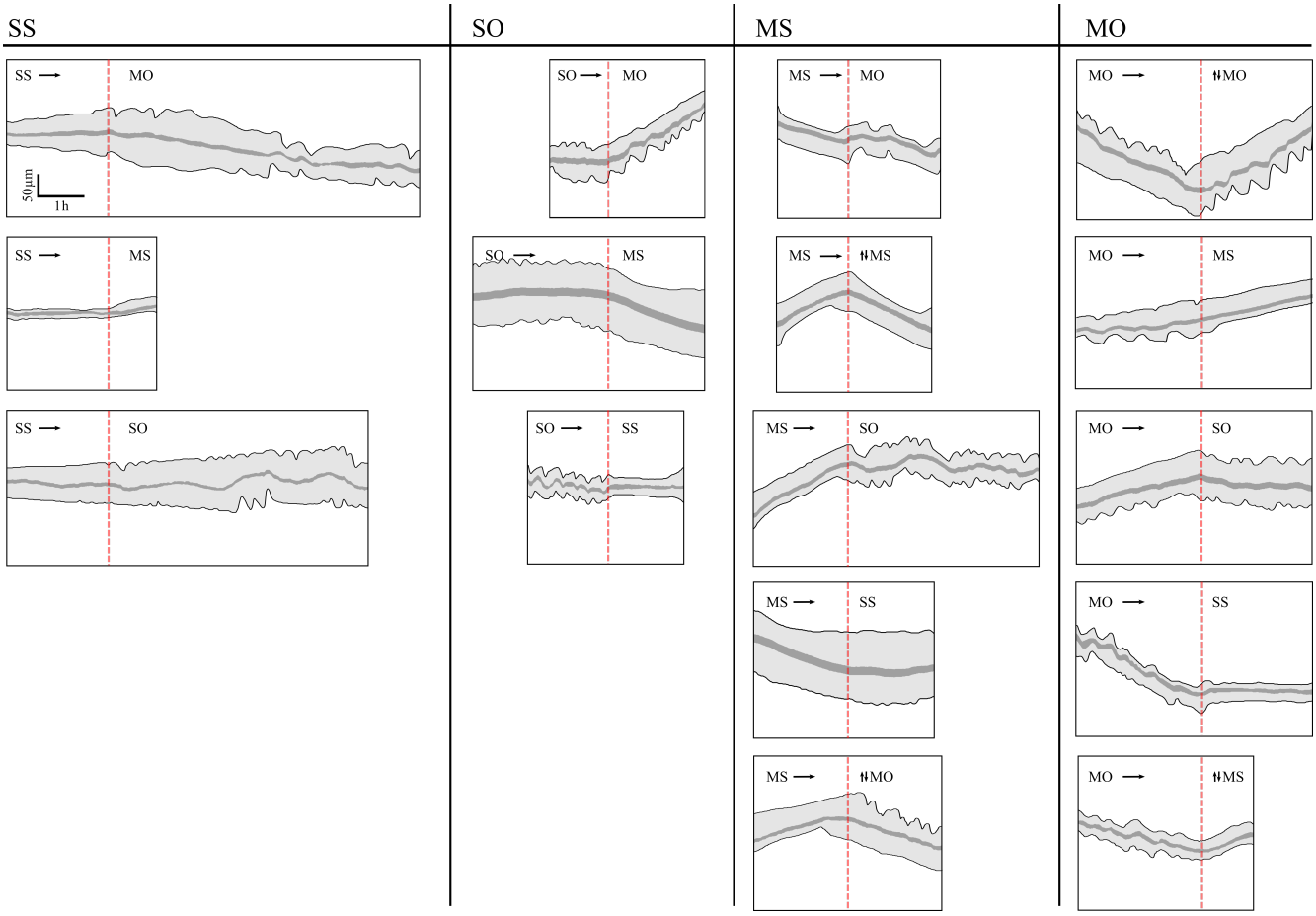

Figure S3: **Examples of all the possible transitions between different states.** Transitions from states SS, SO, MS, and MO are organised in rows. Dashed red lines indicate the time frames of a state transition as determined by the change point algorithm. The scale bars in the top left panel apply to all kymographs. All kymographs are reconstructed form the experimental data set 1_ctrl_30s (see Table S1).

$$O = \frac{1}{n}\sum_{i=1}^{n}\left(|L_{f,i}| + |X_{f,i}|\right)] \tag{S1}$$

O is the oscillation metric, n is the number of time frames of the state, $L_{f,i}$ and $X_{f,i}$ are the band-passed filtered length and cell body position of the cell at time frame i, respectively. We then compare this oscillation metric at each cell episode with a critical value (5 µm). We find this critical value to classify cell states optimally by manual inspection of the cell episodes and their respective values of the oscillation metric. Fig. S2C shows examples of 4 cell episodes with their respective average velocity and oscillation metric values and thus their identified state.

Fig. S3 shows examples of all state transitions in the experimental kymographs. The time points detected by the algorithm as the state change points are shown by dashed red lines.

Fig. S4 shows the average cell velocity in different dynamic states, in experiments and simulations. Cell velocity in the two spread states SO and SS is close to zero. Cell velocity does not change significantly between MS and MO states.

S2.2 Motion metrics

Persistence time is defined as the average time during which a cell body maintains its moving direction on the 1D Fibronectin lanes. We calculate persistence using the low temporal resolution data with time frame intervals of 10 min. We only consider the moving episodes lasting at least two time frames (20 min). With this cutoff, small fluctuations do not affect the persistence calculation.

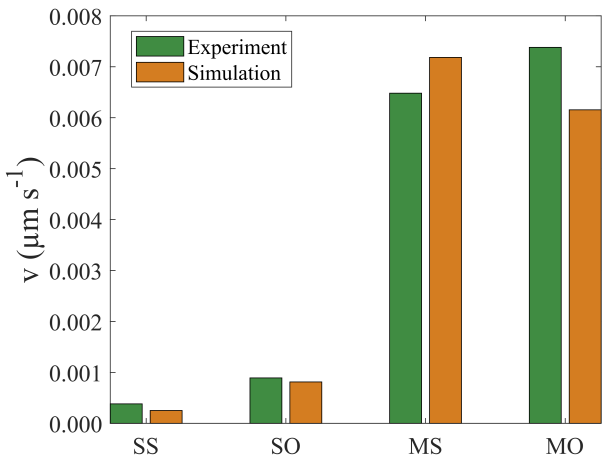

Figure S4: Average cell velocity in different dynamic states of cells in the control condition. The experimental results are obtained from 221 cell tracks with total trajectory time of 2878 h (data set 1_ctrl_30s in Table S1). The simulation results are obtained from 2500 cell tracks with a length of 15 hours each (see section S1.2).

To measure the duration of back excitations (Fig. 5E), we only look into the moving states of the cells. Front and back are then defined according to the direction of movement. We then find the episode of back protruding. The duration of these episodes is averaged over a moving state of a cell. The average velocity of cell body during the moving state is then used to plot Fig. 5E.

We identify collapse events of the front by negative front velocity and a minimal retraction length of 2 μm. The length that the front protrusion shrinks during the complete retraction episode is interpreted as the resistance length in the analysis of the experimental data. We then find the average velocity of the front edge during the protruding episode right before the collapse. This velocity and the shrinkage length during retractions are used to find the experimental relation between front resistance length and velocity (Fig. 5E).

S3 MODEL

Our model describes a cell with front and back protrusion moving on a 1d cell track. Eqs. S2-S4 are the force balance of the mechanical system shown in Fig. 2 for the front(S2), cell body (S3) and back (S4).

$$F_f - E(L_f - L_0) - \zeta_f v_f = 0 \tag{S2}$$

$$E(L_f - L_0) - E(L_b - L_0) - \zeta_c v_c = 0 \tag{S3}$$

$$-F_b + E(L_b - L_0) - \zeta_b v_b = 0 \tag{S4}$$

The force-length relation of the coupling between front and back is well described by an elastic spring (1). This coupling force can be membrane tension or any length-dependent cytoskeletal force. The front and back edge motion experience a drag with the coefficients ζ_f and ζ_b, resp. The cell body velocity is determined by the forces acting on it from front and back protrusion and the drag coefficient of the cell body ζ_c. F_f and F_b in the above equations are defined such that positive sign indicates pushing the membrane out.

The vectorial difference of the edge velocity and retrograde flow velocity v_r is the network extension rate (5). It is fixed by polymerisation, which is force dependent. A few publications motivated us to include this force dependency of polymerisation into our model. Renkawitz et al. (6), Fig. 2A of Maiuri et al. (7) (see also our Fig. S5), and McGrath et al. (8) showed that this dependency is possibly relevant. Koseki et al. explain their experimental results by an exponential dependency of polymerisation rate on single filament load and relate it to the theoretical study by Peskin et al. (9, 10). Bieling et al. measured an exponential dependency like an Arrhenius factor for the single filament polymerisation rate at small forces (11). Network effects like changes in filament density due to branching modify the exponential single-filament dependency at about one quarter of the force-free network extension rate towards less steep decrease (11). Bieling et al. used a system without retrograde flow. Systems

with retrograde flow exhibit much weaker and/or modified density changes, since increasing force also speeds up retrograde flow (6, 12, 13). Another network effect is in some cases binding of filaments to the obstacle surface enabling them to exert pulling forces (6, 14–17). The force dependence has been worked out for a variety of filament-obstacle interaction potentials by Motahari and Carlsson (18). It leads to the well known Arrhenius factor for constant pushing forces (10, 15, 19), which is also a good approximation with a variety of interaction potentials (18). On that basis and on the basis of the low force data in ref. (11) we choose:

$$v_{r,f} + v_f = V_e^0 exp(\frac{-aF_f}{N}) - k^- \tag{S5}$$

$$v_{r,b} - v_b = V_e^0 exp(\frac{-aF_b}{N}) - k^-. \tag{S6}$$

Here, the factor $a = gd/k_BT$ subsumes a factor arising from the average over filament orientation in the network, the length d=2.7 nm added by an actin monomer to the filament and the thermal energy k_BT. N is the number of filaments per edge contour length, and k^- is the depolymerisation rate. We have chosen the value N=248 μm^{-1} in all simulations similar to Schreiber et al. (1). That value entails a/N=1 $\mu m\ nN^{-1}$. An evaluation in retrospect on the basis of our results presented in Fig. S5 showed that the force feedback to network extension rate is not essential in our mechanisms .

The force balancing the drag forces at the protrusion edge is the force $\kappa_f v_{r,f}$ driving retrograde flow (20). With Eqs. S2, S5 and $F_f = \kappa_f v_{r,f}$ we find

$$v_f = \frac{N_f}{a\zeta_f} W_0\left(\frac{V_e^0 a\kappa_f\zeta_f}{N_f(\zeta_f+\kappa_f)} exp\left(\frac{a\kappa_f(k^-\zeta_f - E(L_f - L_0))}{N_f(\zeta_f+\kappa_f)}\right)\right) - \frac{E(L_f - L_0) + k^-\kappa_f}{\zeta_f+\kappa_f}, \tag{S7}$$

and analogously for the back velocity

$$v_b = -\frac{N_b}{a\zeta_b} W_0\left(\frac{V_e^0 a\kappa_b\zeta_b}{N_b(\zeta_b+\kappa_b)} exp\left(\frac{a\kappa_b(k^-\zeta_b - E(L_b - L_0))}{N_b(\zeta_b+\kappa_b)}\right)\right) + \frac{E(L_b - L_0) + k^-\kappa_b}{\zeta_b+\kappa_b} \tag{S8}$$

The retrograde flow velocities $v_{r,f}$ and $v_{r,b}$ can also be written as a function of L and κ

$$v_{r,f}(\kappa_f, L_f) = \frac{N_f}{a\kappa_f} W_0\left(\frac{V_e^0 \kappa_f\zeta_f}{(\zeta_f+\kappa_f)} exp\left(\frac{\kappa_f(k^-\zeta_f - E(L_f - L_0))}{(\zeta_f+\kappa_f)}\right)\right) - \frac{-E(L_f - L_0) + k^-\zeta_f}{\zeta_f+\kappa_f} \tag{S9}$$

$$v_{r,b}(\kappa_b, L_b) = \frac{N_b}{a\kappa_b} W_0\left(\frac{V_e^0 \kappa_b\zeta_b}{(\zeta_b+\kappa_b)} exp\left(\frac{\kappa_b(k^-\zeta_b - E(L_b - L_0))}{(\zeta_b+\kappa_b)}\right)\right) - \frac{-E(L_b - L_0) + k^-\zeta_b}{\zeta_b+\kappa_b} \tag{S10}$$

For simplicity we have chosen the reasonable value $N_f = N_b = 248\ \mu m^{-1}$ entailing $\frac{a}{N_f} = \frac{a}{N_b} = 1$ μm/nN (see also (1)). The velocity of the cell body obeys Eq. S3 as, $v_c = \frac{E(L_f - L_b)}{\zeta_c}$. The length of the protrusions $L_{f,b}$ changes according to the velocity difference between edge and cell body

$$\dot{L_f} = v_f - v_c \tag{S11}$$

$$\dot{L_b} = v_c - v_b \tag{S12}$$

The friction resisting retrograde flow is proportional to the number of transient bonds between the F-actin network and stationary structures in the protrusion. The biphasic relation between retrograde flow velocity and friction forces (5, 21–24) is caused by dissociation of these bonds at high values of the velocity (25). They have to reform to reach their equilibrium density after a high velocity phase. This motivates the bond dynamics (26)

$$\frac{d\kappa_f}{dt} = c_1(\kappa_f^{lim} - (\kappa_f - \kappa_0)) - c_2 e^{\frac{|v_{r,f}|}{c_3}}(\kappa_f - \kappa_0) + \eta_f(t), \tag{S13}$$

$$\frac{d\kappa_b}{dt} = c_1(\kappa_b^{lim} - (\kappa_b - \kappa_0)) - c_2 e^{\frac{|v_{r,b}|}{c_3}}(\kappa_b - \kappa_0) + \eta_b(t), \tag{S14}$$

$$\left\langle \eta_{b,f}(t) \right\rangle = 0 \tag{S15}$$

$$\left\langle \eta_{b,f}(t)\eta_{b,f}(t') \right\rangle = \frac{c_1(\kappa_{b,f}^{lim} - \kappa_{b,f}) + c_2 e^{\frac{|v_{r,b,f}|}{c_3}}\kappa_{b,f}}{\alpha\kappa_{b,f}^{lim}}\delta(t-t') \tag{S16}$$

with an exponential acceleration of bond dissociation by retrograde flow velocity (25). $\kappa_{f,b}^{lim}$ is the upper limit of κ which is determined by the substrate adhesion strength. The terms $\eta_{b,f}$ add Gaussian white noise, arising from the random formation and breaking of bonds of the F-actin network with stationary structures. Our recent study showed that the description of the equilibrium values of $\kappa_{f,b}$ and $\zeta_{f,b}$ by a Hill-type relation with the Fibronectin substrate coating density $B_{f,b,c}$ provided a quantitative description of the adhesion-velocity relation in a single-protrusion model (1). These findings enter the $\kappa_{f,b}$-dynamics by

$$\kappa_f^{lim} = \kappa_0 + \frac{\kappa^{max} B_f^{n_\kappa}}{K_\kappa^{n_\kappa} + B_f^{n_\kappa}}, \qquad \kappa_b^{lim} = \kappa_0 + \frac{\kappa^{max} B_b^{n_\kappa}}{K_\kappa^{n_\kappa} + B_b^{n_\kappa}}. \tag{S17}$$

The drag coefficients ζ at different regions of the cell are:

$$\zeta_f = \zeta_0 + \frac{\zeta^{max} B_f^{n_\zeta}}{K_\zeta^{n_\zeta} + B_f^{n_\zeta}}, \qquad \zeta_b = \zeta_0 + \frac{\zeta^{max} B_b^{n_\zeta}}{K_\zeta^{n_\zeta} + B_b^{n_\zeta}}, \qquad \zeta_c = b\left(\zeta_0 + \frac{\zeta^{max} B_c^{n_\zeta}}{K_\zeta^{n_\zeta} + B_c^{n_\zeta}}\right) \tag{S18}$$

ζ_0 and κ_0 are the base level of the drag coefficient and friction coefficient. The factor b describes the contribution of the cell body to the cell drag compared to the protrusion. Note that relations for the number of bonds and drag at front and back are symmetrical. Eqs. S11-S12, S13, and S14 form a 4th order dynamical system, which determines the cell motility behaviour. We find that our model can reproduce 4 different states of a cell.

Finally, the stationary states of Eqs. S13-S14 exhibit the biphasic friction force - retrograde flow velocity relation discussed in the introduction,

$$F_{f,b} = v_{r,f,b}\left(\kappa_0 + \frac{\kappa^{lim}}{1 + \frac{c_2}{c_1} e^{\frac{|v_{r,f,b}|}{c_3}}}\right), \tag{S19}$$

with the maximum force at $v_{r,cr}$ (see Fig. S10).

S4 THE OSCILLATION MECHANISM AND THE ROLE OF PARAMETERS

Coupled feedback loops are recurring motifs in many biological systems and can cause dynamic behaviors like excitability and oscillations (27). Our model explains how the combination of a positive and a negative feedback loop can give rise to different dynamic behaviors. The dynamics of the friction coefficient κ include a positive feedback mechanism. Chemical noise from random formation of bonds between the F-actin network and stationary structures increases κ from its steady state. Higher friction coefficient slows down the retrograde flow, which in turn reduces the unbinding rate. That leads to even more bonds and higher κ. On the other hand, the length dynamics acts as a negative feedback mechanism for κ. With the increase of κ, retrograde flow decreases, and edge velocity increases. The protrusion length will grow. That increases the elastic force, which resists the growing protrusion. This mechanism tends to decrease the edge velocity and increase retrograde flow velocity. Higher retrograde flow entails higher unbinding, which decreases κ. The dynamic behavior of the cell depends on the relative rates of the positive and negative feedback loops. With appropriate parameter values, the positive and negative feedback loops can work in a coordinated manner, which manifests as oscillations.

We describe here the oscillations of the state SO. The mechanism in the state MO is essentially the same. The spread states are symmetric and it is therefore sufficient to consider one protrusion (without variable indices f, b) as we do in Fig. S5. We start the description of the oscillation cycle in the phase when κ starts to decrease. Retrograde flow v_r increases driven by the force $F_f = E(L - L_0) + \zeta_f v_f$ in this phase (Fig. S5). The increase of v_r causes further decrease of κ due to bond rupture and it continues to fall. Since retrograde flow becomes faster, leading edge velocity v slows down - the growing elastic force due to growing length L brakes additionally. The drag force ζv vanishes with decreasing edge velocity v. At some point, κ is so small that the friction force cannot balance the elastic force anymore. The F-actin network slips with a large peak of v_r. That causes a further and faster decrease of κ. The leading edge follows the network with a negative velocity peak, which rapidly decreases L and the elastic force and F collapse. Retrograde flow has lost its driving force at this moment and v_r and v slow down immediately. Since the elastic force is very small now, the drive for retrograde flow is small and v_r drops very low. The drop of v_r has κ start to rise again, making v_r slow down further. The approximate conservation of the network extension rate has the protrusion velocity go up as v_r decreases (Eq. S5), till the elastic force limits it. That is the time of minimal v_r and maximal v. From that moment on, since v>0 still holds, L and the elastic force continue to grow and speed up retrograde flow. The share of retrograde flow in the network extension rate increases again. The growth of κ stops and turns again into a decline since v_r increases. This closes the loop.

The rates of the positive and negative feedback loops and, thus, the dynamic behavior of the cell depends on the parameter values. Fibronectin density can affect these rates. Increasing B increases κ^{lim}, making the positive feedback loop dynamics

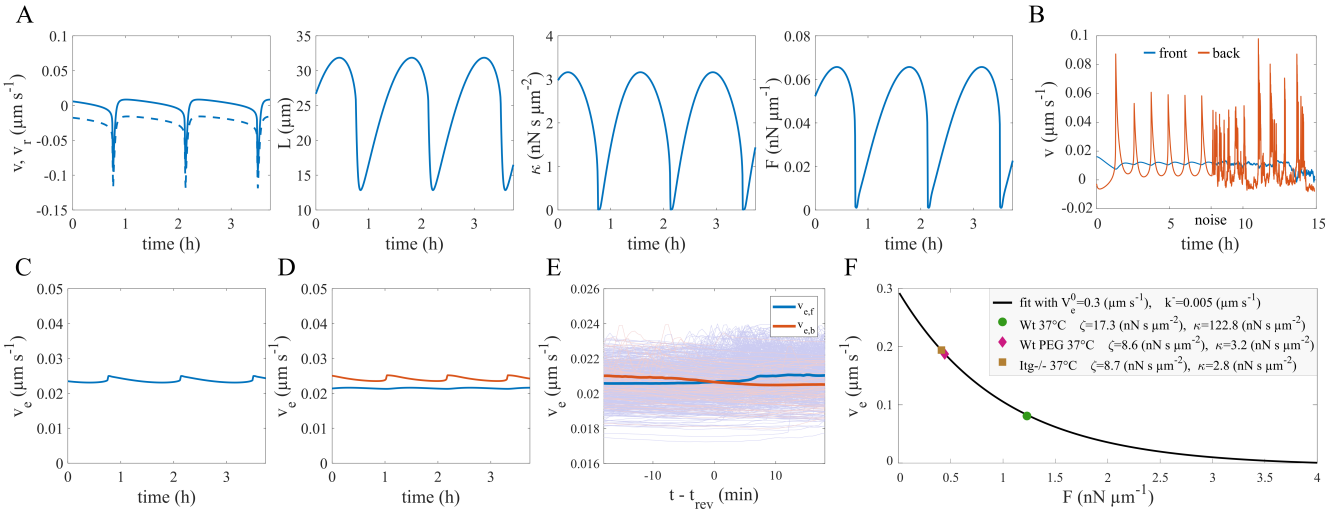

Figure S5: (A) Simulation without noise of the time course of the edge velocity v (full line), retrograde flow v_r (dashed line), cell length L, friction coefficient κ and force on the edge membrane F in state SO. Front and back protrusion behave identical in deterministic simulations of this state. (B) The simulation in the state MO starts deterministic and then switches on the noise (blue front, orange back). Remarkably, the average frequency of the noisy oscillations is higher than the deterministic one. The deterministic oscillations are most similar to the smooth experimental example in Fig. 3A, the noisy oscillations are more similar to the noisy oscillations in Fig. 1. (C,E) Time course of the network extension rate in the simulation without noise of the state SO (C) and MO (D) and as average over many simulations during a direction reversal event (E). Its changes are very small. Consequently, the force dependency of polymerisation is not an essential feedback in our oscillation and direction reversal mechanisms. The results in A-C and D are obtained from simulations of SO and MO states in Fig. 3, resp. Simulations in A-D use parameter values of set 1 listed in Table S2 with $c_3 = 8.8\ \mu\text{ms}^{-1}$. The Fibronectin density B in panels A-C and D are $36\ \text{ng cm}^{-2}$ and $80\ \text{ng cm}^{-2}$, resp. The results in E are obtained from simulations similar to Fig. 5A with the parameter values of set 1 listed in Table S2. (F) Maiuri et al. (7) present in their Fig. 2 data not obeying the UCSP. We consider here the data from this figure measured at 37°C. The green dot shows control data ($v = 0.071\ \mu\text{ms}^{-1}$, $v_r = 0.01\ \mu\text{ms}^{-1}$). The other two dots show conditions with substantially increased retrograde flow velocity due to reduced interaction between retrograde flow, actin cortex and substrate by either lack of Fibronectin ligand (PEG, purple, $v = 0.051\ \mu\text{ms}^{-1}$, $v_r = 0.138\ \mu\text{ms}^{-1}$) or integrin knock out (Itg-/-, brown, $v = 0.047\ \mu\text{ms}^{-1}$, $v_r = 0.146\ \mu\text{ms}^{-1}$). We have fit these 3 data points to Eq. 4 of Schreiber et al. (1) providing the relation between friction coefficient κ, cell drag coefficient ζ and cell velocity, and to the Eq. S5 for the dependency of the network extension rate on force (black line). The force-free network extension rate V_e^0, κ and ζ are the fit parameters. In agreement with the experimental conditions, both κ and ζ are substantially reduced with PEG and Itg-/-. The force-feedback to network extension rate is relevant here, since the network extension rate changes by about a factor 3 compared to control while the value of V_e^0 is the same for all three conditions. The relevance of this feedback has also been suggested by Renkawitz et al. (6).

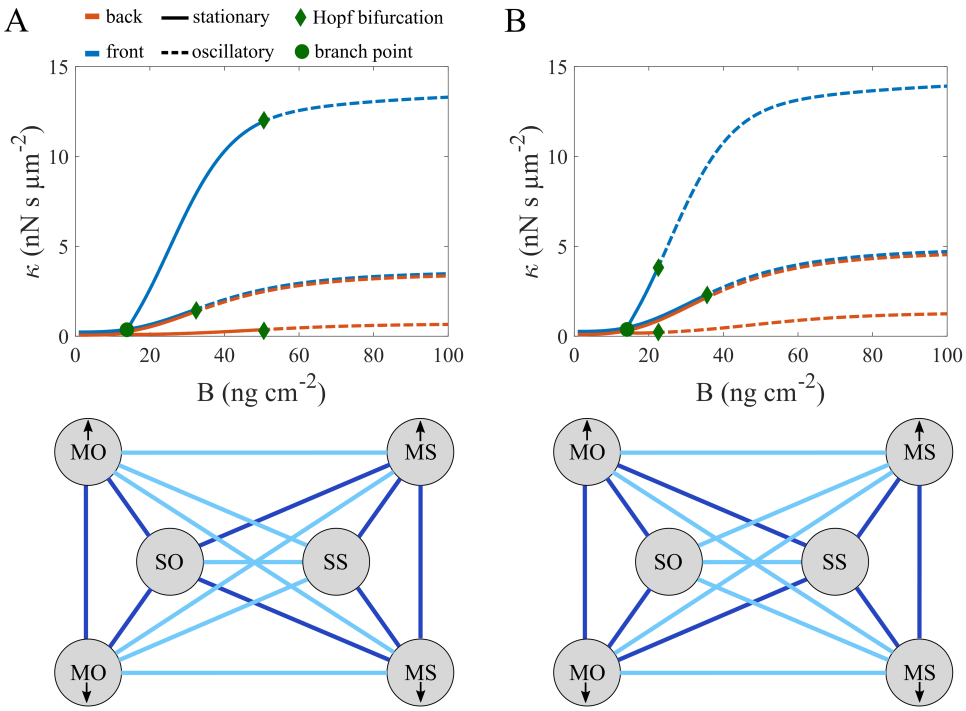

Figure S6: **The dynamic cell states and transitions between them with 2 different parameter value sets.** The upper row shows the cell states of the noise-free model illustrated by their value of the friction coefficient κ for a range of Fibronectin density B. Dashed lines show oscillatory states. The lower row shows the possible transitions between cell states when noise is added to the model. Dark blue lines show the transitions between states coexisting in the noise-free model. The parameter values in (A) are taken from set 1, Table S2. In (B), the value of the parameter c_3 is 5% higher and the one of V_e^0 is 5% lower than the values of set 1.

faster. The positive feedback loop will amplify a sufficiently large perturbation caused by noise in the κ dynamics before getting damped out by the negative feedback loop. In this situation, protrusions are excitable. At even higher values of B, the positive and negative feedback loops work in a coordinated oscillatory manner.

Other parameters of the cell can also influence feedback loops. In particular, the rate of the negative feedback loop through length dynamics depends mainly on the parameters E and V_e^0. On the other hand, the rate of the positive feedback loop (κ dynamics) is mainly dependent on the rates c_1 and c_2. Also, the parameter c_3, which scales the sensitivity of the unbinding rate to the retrograde flow velocity, is a critical parameter in determining the state of the cell. Changing c_3 affects the order of Hopf bifurcation points on moving and stationary state branches (Fig. S6), which makes different state transitions possible. That can explain the observation of different state transitions by cell-to-cell variability (see section S6).

S5 BIPHASIC ADHESION-VELOCITY RELATION

The adhesion velocity relation has been measured in untreated cells (data set 7_untreated_10min). We used the control parameter value set 1 (Table S2) for these simulations. We averaged the velocity over the whole population in the experiments at a given Fibronectin density. We find a biphasic relation with maximal cell velocity at intermediate Fibronectin densities, as in Schreiber et al. (1). We find that our simulations for control condition (parameter value set 1 in Table S2) can reproduce the biphasic adhesion-velocity-relation observed in the experiments (Fig. 2 B). Similar to (1), we find saturation of the velocity at large Fibronectin densities in simulations and experiments. This shows that our model with two protrusions also reproduces the biphasic adhesion-velocity relation which is a general experimental observation with many cell types.

S6 REMARKS ON OTHER POSSIBILITIES FOR THE COEXISTENCE OF STATES

In Fig. 3C, we showed the coexistence of SO and MS states in a range of Fibronectin densities (see also Fig. 4A). This is caused by the fact that the Hopf bifurcation of the moving state occurs at higher Fibronectin density (B) than the Hopf bifurcation on

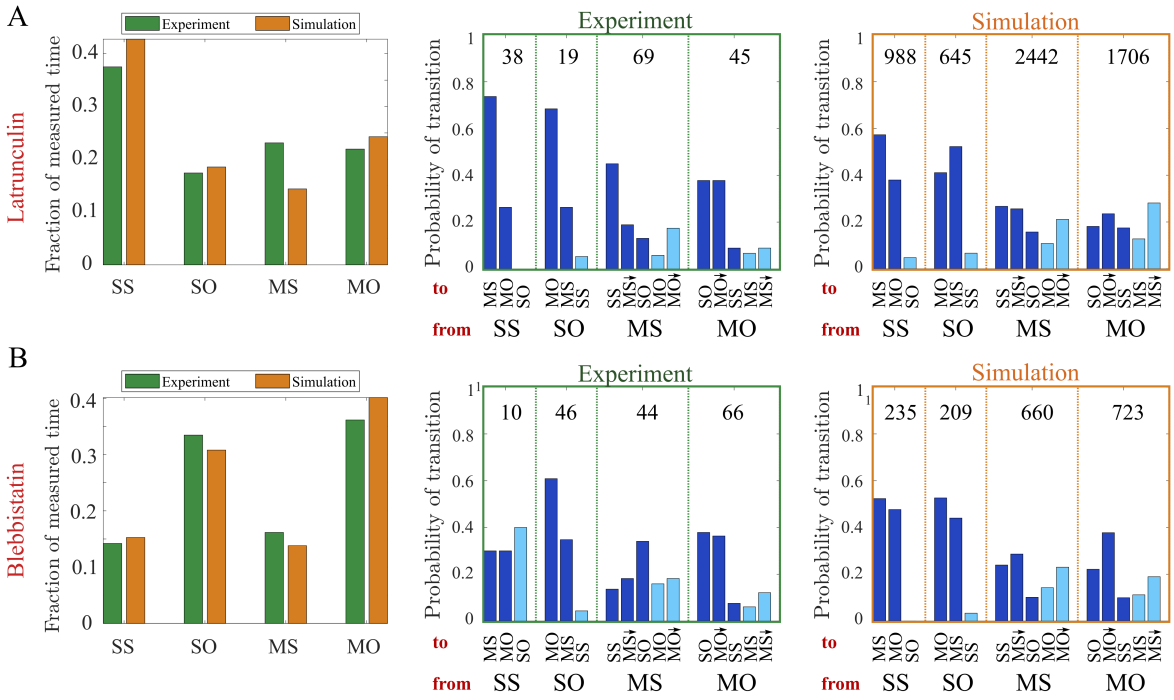

Figure S7: **Analysis of dynamic cell states and transitions in Latrunculin A (A) and Blebbistatin (B) treated cells.** Left column: Fraction of cells in the dynamic cell states in experiments and simulations in a range of Fibronectin densities. Middle column: Statistics of state transitions in experiments. Right column: Statistics of state transitions in simulations. The parameter values of data sets 2 and 3 (Table S2) are used for Latrunculin A and Blebbistatin simulations, respectively. Sample size is indicated by the numbers inside the chart.

the spread branch. The possible state transitions for this case is shown in the bottom panel of Fig. S6A. The order of Hopf bifurcation points on the moving and spread branches of Fig. 3C may be different for another cell described by a slightly different set of parameter values within the range ±5% of parameter values we use to account for cell variability (see section S1.2). Fig. S6B shows a case in which the Hopf bifurcation of the spread state occurs at higher Fibronectin density, and thus SS and MO states coexist in a range of B. We used the parameter values of set 1 in Table S2 and only slightly changed the parameter c_3 and V_e^0 for this case. Possible state transitions are illustrated in the lower panel of Fig. S6B for this case. This shows that cells with slightly different parameter values can experience different transitions. In summary, due to cell-to-cell variability within a given experiment, we find a larger variety of coexistence options than indicated by a single bifurcation scheme.

S7 REMARKS ON THE EFFECT OF THE DRUG TREATMENTS ON STATES AND TRANSITIONS AND PERSISTENCE

Fig. S7A and B show the probability of states and transitions for Latrunculin and Blebbistatin-treated cells. We find that the application of Latrunculin increases the fraction of cells in the spread states compared to control condition (Fig. 3B). The fraction of steady states relative to the oscillatory states is also increased. The simulations in Fig. S7A show good agreement with the measurements. Only the network extension rate V_e^0 is decreased relative to control parameter values in Latrunculin simulations (Table. S2) which corresponds to the effect of the drug on the system. Thus, lower probability of oscillatory and moving states is a result of lower network extension rate. Also the probabilities of state transitions in the simulations show good agreement with the measurements in the Latrunculin-treated cells. Fig. S7B shows that the fraction of states in Blebbistatin-treated cells is almost similar to the control condition.

Blebbistatin application does not change the UCSP qualitatively. We find that persistence time increases with cell velocity also in the Blebbistatin-treated cells (Fig. S8). Application of Blebbistatin increases the persistence time compared to control, but not as much as the Latrunculin application. The simulations of the Blebbistatin condition show good agreement with the measurements (Fig. S8).

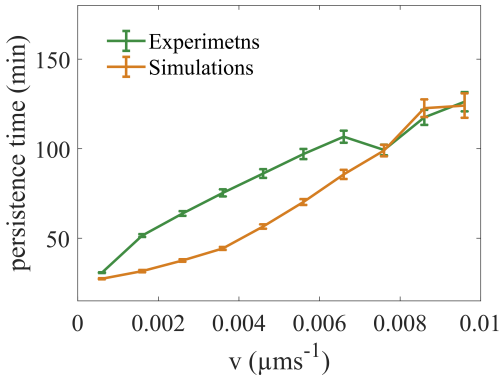

Figure S8: The relation between cell velocity and persistence time with Blebbistatin applied (modeled by parameter values of set 3 in Table S2).

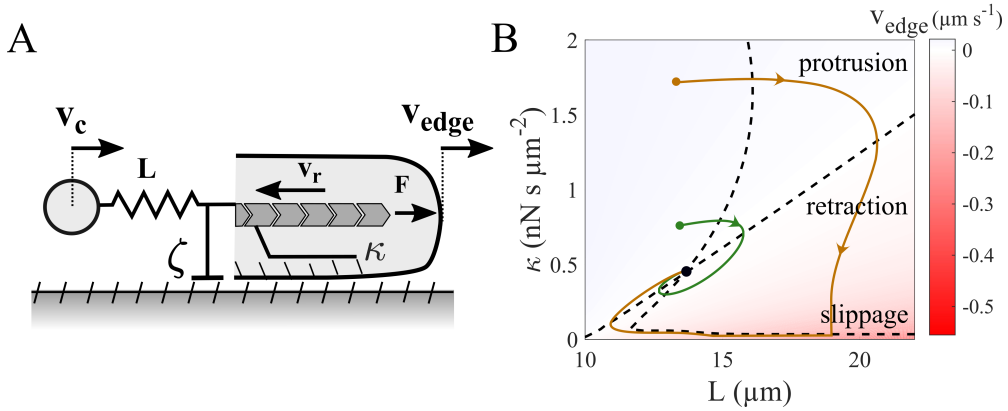

Figure S9: (A) **Schematic illustration of the model for one protrusion.** Here (v_c) is a model parameter which comprises the effects from the other cell parts on the protrusion. (B) **The phase plane of the spread state case** ($v_c = 0$)**.** Two black dashed lines show the nullclines of the system. Green and orange lines are two example trajectories in the phase plane of the noise-free model; one goes smoothly to the stable state (green), and one goes to the stable state through a slippage retraction (orange). The background colour indicates the velocity of the cell edge. Above and below the diagonal line the edge is in protrusion and retraction, respectively. The bottom right corner of the plane is associated with slippage phenotype. The parameter values of set 1 (Table S2) are used with B = 20 ng cm^{-2} for the phase plane in this figure.

S8 EXCITABILITY AND STABILITY OF A PROTRUSION IN THE CELLULAR STATES SS AND MS AS SEEN BY DYNAMIC SYSTEMS THEORY

Dynamic systems theory uses the terms 'state' and 'phase space' to characterise system behaviour rather than plots of dynamic variables in dependence on time. A state of a system is completely described by the value of its dynamic variables[1]. A dynamic variable obeys a differential equation fixing its dynamics. A dynamical system has as many dynamic variables as ordinary differential equations describing it. Each dynamic variable defines one dimension (or coordinate axis) of the phase space. A point in the phase space corresponds to a state of the system. We have 4 dynamic variables: κ_f, κ_b, L_f and L_b.

We consider steady protrusions in the cellular state SS and MS in this section. If the protrusions are very weakly coupled, it suffices to consider a single protrusion, which has the 2 dynamic variables κ and L. With this assumption, the effect of the other cell parts (the cell body and the protrusion at the other end of the cell) on the protrusion is included in the parameter v_c (Fig. S9A). Specifying the model to this situation leads to

$$\frac{d\kappa}{dt} = c_1(\kappa^{lim} - (\kappa - \kappa_0)) - c_2 e^{\frac{|v_r|}{c_3}}(\kappa - \kappa_0) \tag{S20}$$

[1]Our use of the term 'cell state' for SS, MS, SO, MO deviates from this definition. The four cell states correspond to dynamic regimes in terms of dynamical systems theory.

$$\frac{dL}{dt} = v - v_c = \frac{1}{\zeta} W_0\left(\frac{V_e^0 \kappa \zeta}{(\zeta+\kappa)} e^{\frac{\kappa(k^-\zeta - E(L-L_0))}{(\zeta+\kappa)}}\right) - \frac{E(L-L_0) + k^-\kappa}{\zeta+\kappa} - v_c \tag{S21}$$

$$v_r(\kappa, L) = \frac{1}{\kappa} W_0\left(\frac{V_e^0 \kappa \zeta}{(\zeta+\kappa)} e^{\frac{\kappa(k^-\zeta - E(L-L_0))}{(\zeta+\kappa)}}\right) - \frac{-E(L-L_0) + k^-\zeta}{\zeta+\kappa} \tag{S22}$$

Its phase space is the L-κ-plane, shown in Fig. S9B for a spread model cell (v_c=0). The dashed lines in Fig. S9 are called nullclines, and mark those L and κ values for which either $dL/dt = 0$ or $d\kappa/dt = 0$ holds. At their intersection point, both dynamics are 0, and the state does not change, i.e., it is an equilibrium state. If the system starts at any state except the equilibrium state, it moves towards the equilibrium state, and draws its trajectory in phase space.

Fig. S9 shows two example trajectories. The green one starts rather close to the stationary state at $\kappa \approx 0.5$ nNsμm^{-2}, L=20 μm. It quickly moves to the equilibrium state. The orange trajectory starts at $\kappa \approx 1.9$ nNsμm^{-2}, L=20 μm. It starts on a flux line first leading to much larger L - the protrusion grows. It then turns to very small values of κ, where it turns parallel to the $\dot{\kappa}$-nullcline, and L decreases even below the stationary value - the protrusion retracts. This retraction is fast, since it happens at small κ, and corresponds to a slippage event. Slippage events occur whenever the system reaches this low-κ branch of the $\dot{\kappa}$ nullcline. Finally, the trajectory approaches the equilibrium state. The large amplitude of the initial protrusion growth and the slippage event set the orange trajectory apart from the green one on a phenomenological level. We introduced a basin of attraction in Fig. 5C, to distinguish the trajectories going directly to the equilibrium state from the trajectories including slippage.

S9 FORCE-RETROGRADE FLOW REGIMES AND DIRECTION REVERSAL

Eq. S19 shows that force has a biphasic relation with the retrograde flow in the stationary state. Thus, change of force upon variation of retrograde flow depends on the regime that the protrusion is working in. Retrograde flow is not symmetric in a moving cell. It is the vectorial sum of extension rate and edge velocity (Fig. 5F). This entails higher retrograde flow at the cell back. The right panel in Fig. S10 shows the retrograde flow in the simulations during a direction reversal. In the beginning, the retrograde flow at the back is higher than at the front. This changes after the reversal swapping the roles of front and back. We find that the retrograde flow at the front is always lower than $v_{r,cr}$, and thus working in the rising branch of force - retrograde flow relation (Fig. S10, left). However, on the other side of the cell, back retrograde flow is always higher than $v_{r,cr}$. The faster the cell moves, the larger is the separation between the retrograde flow at the front and back protrusions.

The left panel in Fig. S10 shows that both protrusions in a slow cell work close to the critical retrograde flow rate, $v_{r,cr}$. Reversal of the direction requires switching the roles of front and back. Thus, the reversal should be easier in slow cells, whose protrusions work close to the $v_{r,cr}$. This argument agrees with the lower persistence time and higher reversal probability of slow cells.

Differences in the force-retrograde flow regime lead to a characteristic difference between the front and back protrusions. The retrograde flow rate has positive feedback on force generation at the front. It speeds up at the front, if the front edge motion is slowed down due to back pulling. This increases the force generation at the front, which tends to oppose the velocity reduction caused by the pulling of the back. However, the retrograde flow rate has a negative feedback on the force generation at the back. If the back edge speeds up due to the stronger front pulling, the back retrograde flow also speeds up. As a result, the back force resisting motion decreases. In this sense, the back even helps the front pulling to increase the cell velocity.

To see how the force-retrograde flow regimes change during a reversal, we perturbed the friction coefficient κ at the back to induce a cell reversal. Fig. S11A shows a case when the perturbation is not large enough and cannot trigger the reversal. The panel on the bottom shows the evolution of back and front protrusions in the force-retrograde flow plane. The perturbation at the back is not sufficiently large. So, front and back states eventually return to their original locations on the biphasic curve of the steady states. Fig. S11B shows a case with a sufficiently large perturbation that can induce the reversal. The panel on the bottom shows how the back state moves from the falling branch to the rising branch of the biphasic steady state curve. Fig. S11C shows the flux lines in this F-v_r plane. Although they are obtained from the single protrusion model with the assumption that the velocity of the cell body stays unchanged, they can still approximate the behaviour of the full model. The flux lines are shown for a front protrusion (upper panel), a protrusion in the spread state (middle panel), and a back protrusion (bottom panel). In a front protrusion, the flux lines converge to a fixed point on the rising branch of the biphasic steady state force-retrograde flow curve. The fixed point is on the falling branch of the steady state curve in back and spread protrusions.

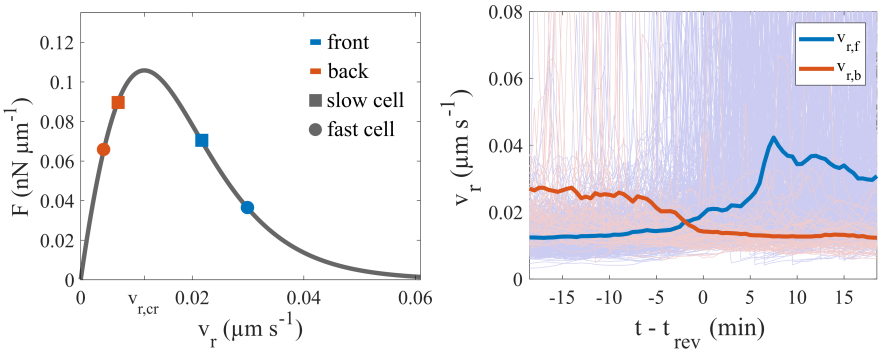

Figure S10: Left: **The biphasic relation between force and retrograde flow in the stationary state.** $v_{r,cr}$ is the critical flow rate with maximal force. Symbols show the steady state retrograde flow and force at the back and front protrusions for a fast and a slow cell. Right: **Retrograde flow at front ($v_{r,f}$) and back ($v_{r,b}$) protrusions during a direction reversal** as average over many simulated cell tracks (thin lines). t_{rev} is the time when the cell nucleus changes direction. The results are obtained from simulations similar to Fig. 5A with the parameter values of set 1 listed in Table S2.

S10 STATIONARY FORCE-VELOCITY RELATION OF CELL MOTION AND STALL FORCE

To determine the stationary force-velocity relation of cell motion, we include an external force acting on the leading edge membrane of the cell, F_m in our formulation. The force balance at the leading edge gives:

$$F_f - E(L_f - L_0) - \zeta_f v_f - F_m = 0 \tag{S23}$$

With that, Eq. S7 changes to:

$$v_f = \frac{N_f}{a\zeta_f} W_0\left(\frac{V_e^0 a\kappa_f\zeta_f}{N_f(\zeta_f+\kappa_f)} exp\left(\frac{a\kappa_f(k^-\zeta_f - E(L_f-L_0) - F_m)}{N_f(\zeta_f+\kappa_f)}\right)\right) - \frac{E(L_f-L_0)+F_m+k^-\kappa_f}{\zeta_f+\kappa_f}, \tag{S24}$$

We use Eq. S24 instead of Eq. S7 together with all the other equations to find the cell velocity in the stationary state in dependence on F_m. Fig. S12 shows velocities and forces in dependence on the external force. We present the deterministic relation without noise here to be comparable to earlier published predictions. Cell velocity decreases with increasing F_m, but in two different regimes. At low F_m, front retrograde flow speeds up with increasing F_m, due to the decrease of the leading edge membrane velocity caused by the opposing external force. At a certain F_m the front retrograde flow comes very close to the critical value $v_{r,cr}$ (Fig. S12, middle). In this situation, the protrusive force at the front F_f reaches the maximum force that the protrusion can produce (see the biphasic force-retrograde flow relation in Fig. S11). F_f cannot increase more after this point by increasing F_m (Fig. S12, right). Thus, the stationary force velocity relation enters a new regime, with saturated protrusive force:

$$v_f = \frac{1}{\zeta_f}\left(\kappa_f v_{r,cr} - \left(E(L_f - L_0) + F_m\right)\right) \tag{S25}$$

Increasing F_m in this regime decreases the velocity almost linearly with small deviations from linearity arising from the interaction of all mechanical components. Cell motion stalls when $\kappa_f v_{r,cr} = E(L_f - L_0) + F_m$ is reached.

Mathematical models of cell motion with linear friction of retrograde flow predicted a linear stationary force-velocity relation or piecewise linear relation very similar to Fig. S12 (1, 28). Here, we find also a monotonously decreasing function (in difference to the non-monotonous dynamic force-velocity relation reported in (20, 29, 30)). Model predictions for the stationary relation agree in the point that this relation reflects the retrograde flow friction law. These model predictions are in agreement with the stalled state of the dynamic force-velocity relation, since the stall force is determined by retrograde flow (20). The stationary force-velocity relation thus provides access to the 'internal' property retrograde friction law from 'outside'. While the dynamic relation has been measured and analysed in detail (20, 29, 30), the stationary force-velocity relation has not been measured, yet.

S11 STIMULATING DIRECTION REVERSAL BY FIBRONECTIN STEPS

In order to substantiate the picture of competing protrusion and the concomitant probabilities of reversals, we designed an experiment where cells experience an abrupt change in the parameter B as a Fibronectin density step. Additional motivation

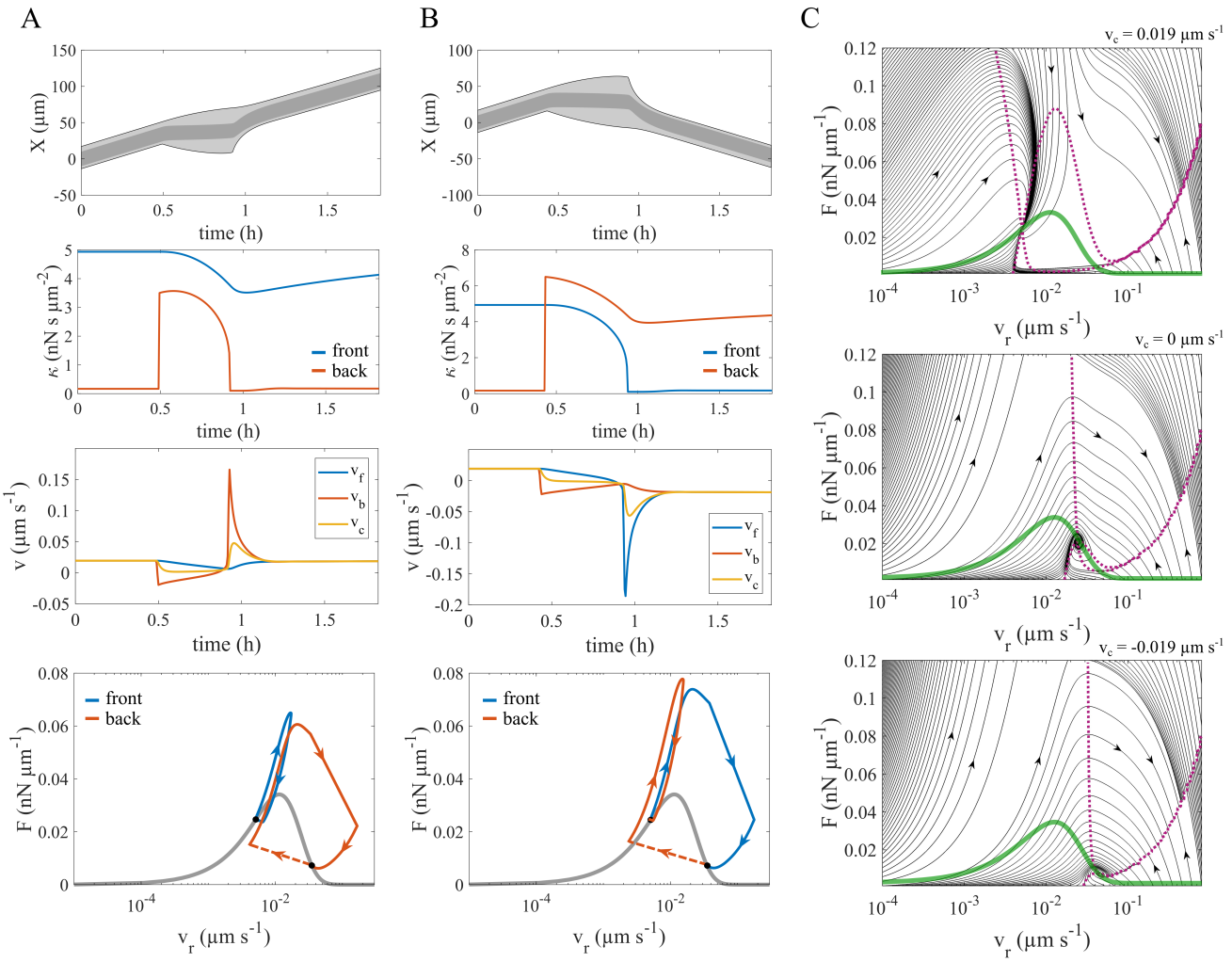

Figure S11: **The behaviour of force and retrograde flow at the front and back protrusions during a direction reversal.** (A) Cell evolution during a back excitation that does not lead to a reversal. Kymograph, friction coefficient κ, and velocity of the cell front (blue) and back (red) are shown during the back excitation. The back excitation is started by an instantaneous increase of κ in a simulation without noise. The lower panel shows the evolution of front and back in the force-retrograde flow plane. The dashed part of the red line indicates the perturbation of κ at the back. The grey line shows the steady state biphasic relation between force and retrograde flow. (B) Cell evolution during a back excitation that leads to a reversal. Kymograph, friction coefficient κ, velocity, and the trajectory in the force-retrograde flow plane are shown as in (A). (C) Flux lines in the force-retrograde flow plane. They are obtained using the model for a single protrusion (S8) with the positive (up), zero (middle), and negative (bottom) cell velocity. The green line shows the biphasic force-retrograde flow relation in the stationary state. Purple dotted lines show the nullclines of the system in the F-v_r plane. The parameter values of set 1 (Table S2) are used with B = 20 ng cm^{-2} for the simulations in this figure.

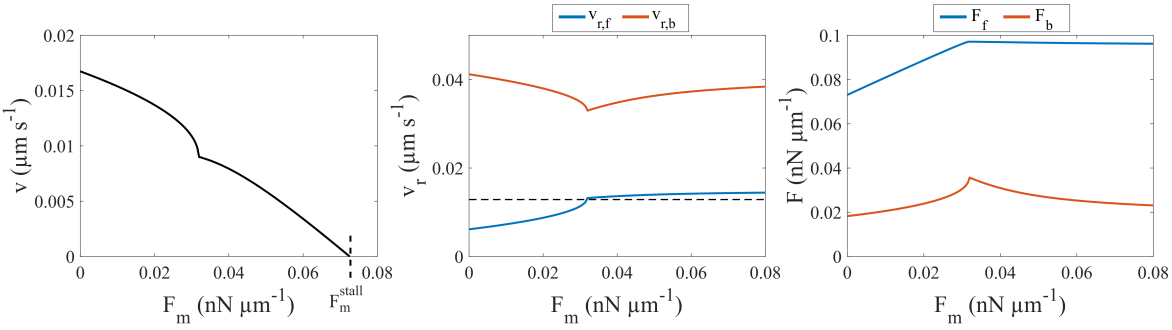

Figure S12: **Stationary force-velocity relation.** Left: The relation of cell velocity v and external force F_m in the noise-free model. The cell stalls at the force F_m^{stall}. Middle: Retrograde flow v_r at the front and back protrusions in dependence on F_m. The dashed line indicates the critical velocity $v_{r,cr}$ of the relation between friction force and retrograde flow velocity with maximal force (see section S3.) Right: Force at the front and back protrusions F in dependence on F_m. The parameter values of set 1 (Table S2) are used in this figure. The Fibronectin density B is assumed to be 45 ng cm^{-2}.

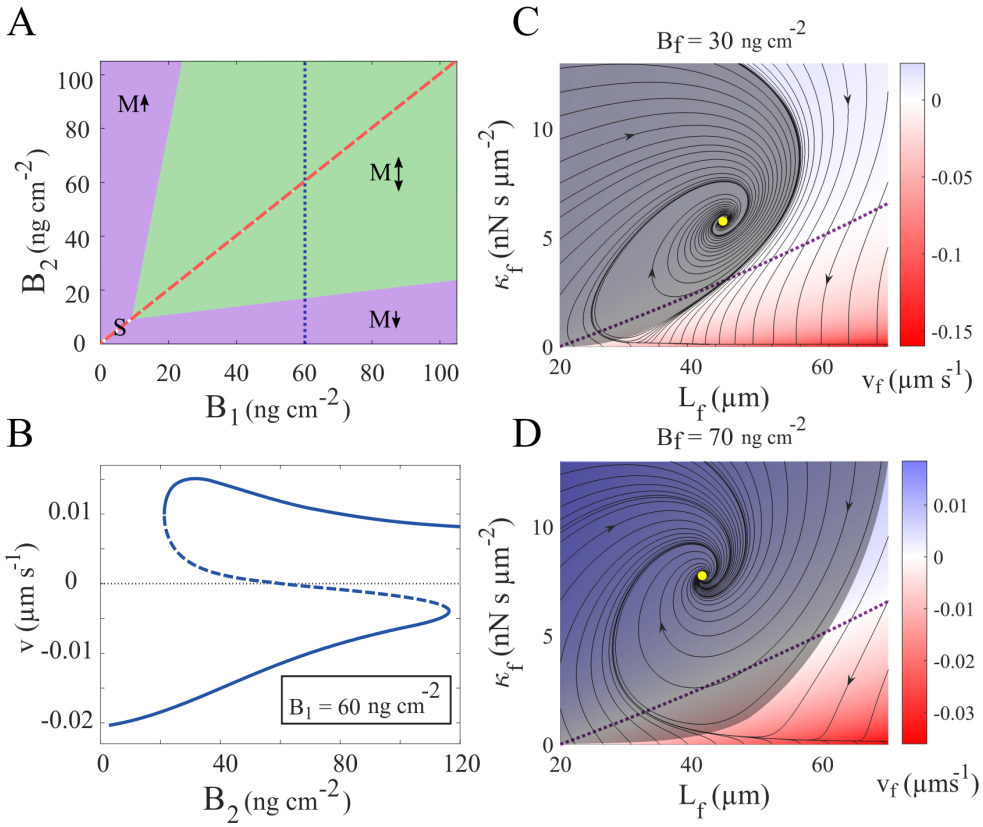

Figure S13: **Cell states on FN steps.** (A) 2D bifurcation diagram with respect to Fibronectin densities forming the step B_1 and B_2. Cells can move only in one direction in the purple regions. Both upward and downward states coexist in the green region. (B) Cell states illustrated by their value of the cell velocity for a range of Fibronectin densities at the cell front B_2. The Fibronectin density at the cell back B_1 is 60 ng cm^{-2}. This corresponds to the blue dotted line in panel A. (C), (D) The basin of attraction of the steady protrusion state (grey area) and state trajectories (black lines) in κ-L plots. The dotted purple lines represent zero velocity. The parameter values of set 4 (Table S2) are used in this figure.

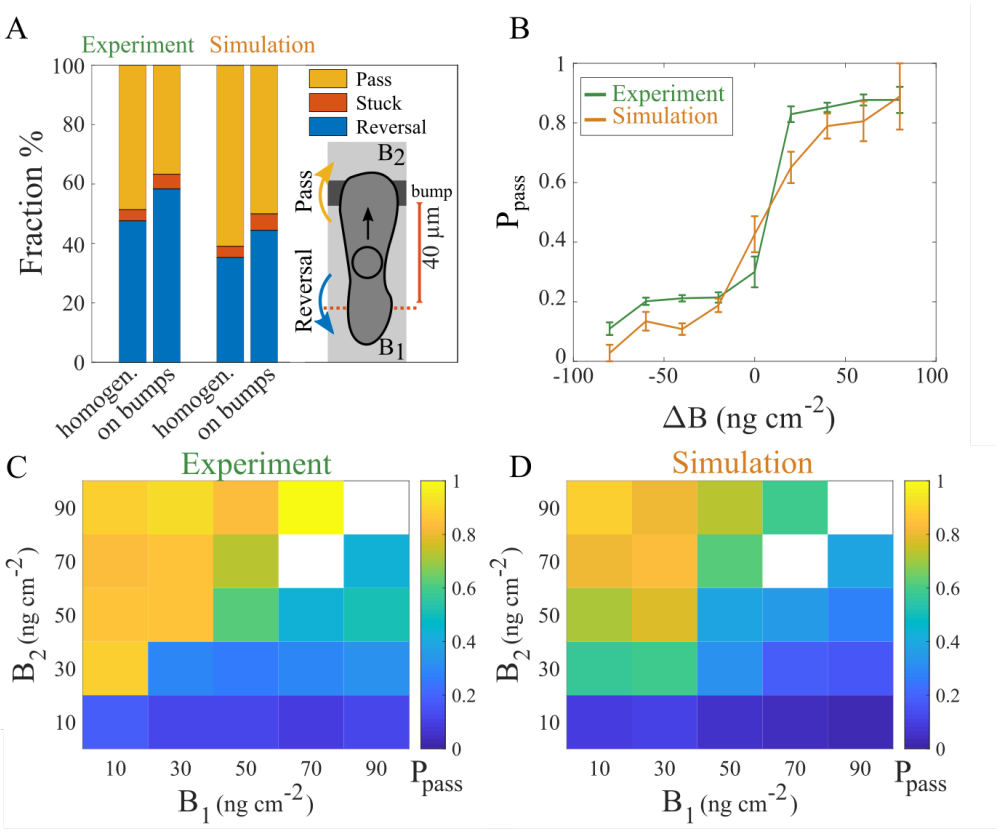

Figure S14: **Cell behaviour at Fibronectin steps.** (A) Examples for the probabilities of the three choices passing, reversing direction and getting stuck on a homogeneous area and at a Fibronectin 'speed bump' of about 10 ng cm^{-2} and 10 µm width. We observe the nucleus when it enters a 40 µm range before the step. If it leaves the range on the side it entered, it is a direction reversal, if it leaves across the step, it is a pass, and if it remains longer than a dwell time of 5.5 h in this range, it got stuck. The choice of this dwell time is according to our definition of a spread cell. (B) The probability to pass P_{pass} in relation to the step height averaged over a range of initial densities from 0 to 100 ng cm^{-2}. (C), (D) P_{pass} for all measured pairs of B_1 and B_2. Cells move from B_1 into B_2. White colour indicates data not measured. The parameter values of set 4 (Table S2) are used for the simulations in this figure.

for experiments on heterogeneous lanes arise from the heterogeneous adhesion strength cells moving in organisms during development, metastasis or wound healing experience. MDCK cells may even modify ligand density by Fibronectin deposition and thus spatially constraint their motion (31). We address these observations by investigating cell behaviour at adhesion steps.

A cell can be perceived as a bistable system within a range of step heights around 0 (Fig. S13A, B). Unlike the homogeneous lanes of Fibronectin, the adhesion density beneath the cell front and back are not equal on the Fibronectin steps. We performed a two-parameter bifurcation analysis on the cell in this situation with parameters B_1 and B_2 being the Fibronectin concentrations forming the step. The Fibronectin density at the cell body B_c is assumed to be the average of B_1 and B_2.

Fig. S13A shows results of the bifurcation analysis. Cells are in a bistable regime allowing for motion in both directions in the green region. Hence, cells do not necessarily move towards the higher Fibronectin fields, even in the noise-free model. Except on very large Fibronectin steps (purple regions) cells have both up-moving and down-moving stable states. Hence, the concept of multistability also explains the crossing of Fibronectin steps.

The absolute values of the velocity in either direction are not equal with a cell on a step. The speed with which the cell moves into the area with higher adhesion is different from the speed in opposite direction. Applying our concept of the basin of attraction reveals that the front protrusion of a cell moving into a higher-adhesion area is more stable than the one of a cell moving into a lower-adhesion area (Fig. S13C, D).

A cell facing a step has three choices: passing the step, turning around or getting stuck (Fig. S14A). A small Fibronectin step of 10 ng cm^{-2} changes the probabilities for all three choices already. Fig. S14B shows that cells like to move into high-adhesion areas (positive ΔB). This is in agreement with our calculation of larger stability of front protrusions during the transition than during motion in the opposite direction. This preference for high adhesion density is in agreement with haptotaxis and the restriction of cell motion by Fibronectin deposition mentioned above. However, cells are also able to move into low-adhesion areas (negative ΔB), and thus do not get stuck in places with high adhesion.

Remarkably, cells do not pass with certainty even on large steps up the Fibronectin concentration. A small probability for reversal remains. This observation can be comprehended with the concept of the cell on a step being a bistable system where noise may cause transition to either state.

We could again reach good agreement between experimental data and simulations for each of the data sets presented in Fig. S14. Hence, the set of ideas defining the theory is also able to explain the motion of cells across Fibronectin steps.

S12 REMARKS ON UCSP SIMULATIONS

The persistence time is defined as the time the nucleus of a cell moves continuously in the same direction. The *Instantaneous velocity* of the cell has been determined from the nucleus position of consecutive frames without any averaging over several time steps or cutoffs. The *velocity* is the difference of positions of consecutive direction reversions divided by the difference of the points in time of these reversions. The data in Fig. 5B are the average over all the cell trajectories in each condition.

A histogram of the persistence time of the moving episodes shows that the reversion of the direction is a Poisson process. To determine persistence time and the corresponding velocity, we analysed data sets with two different time resolutions (10 min and 30 s). The same temporal resolutions and Fibronectin densities are used in the corresponding simulations to determine persistence time and instantaneous velocity. All other parameters in the simulations are the same as Table S2, set 1. With this definition, persistence time is dependent on the temporal resolution of the cell measurement. The calculated persistence time is shorter for data with higher temporal resolution because occurrence of one small time step with displacement in the opposite direction is more likely than a large time step with reversed displacement. The low temporal resolution of 10 min removes the effect of the small fluctuations of the nucleus position on the determination of persistence length, while the high temporal resolution captures these fluctuations. Different velocities of moving episodes are caused by the noise in the system. We find that there is a positive correlation between cell velocity and the persistence time (Fig. 5B). However, they are exponentially correlated only in the low velocity range. The persistence time and velocity show similar dependency in the drug treatment experiments.

S13 IDEAS OF MORPHODYNAMIC MECHANISMS IN MDA-MB-231 CELLS DISCUSSED IN LITERATURE

d'Alessandro et al. showed with MDCK epithelial cells that Fibronectin deposited by the cells themselves during motion might generate a range of increased Fibronectin density on the substrate (31). MDCK cells on 1d Fibronectin lanes like to stay within the region where they increased the Fibronectin density, and only leave it after having turned around several times at its boundaries. d'Alessandro et al. explain their observations by cells shying away from passing Fibronectin steps down. This observation agrees with our results on behaviour of MDA-MB-231 cells on artificial Fibronectin steps. The bistable behaviour of cells on steps explained in section S11 offers a mechanistic explanation. The probability to pass steps towards

lower Fibronectin density is small (Fig. S14B), i.e. cells turn around more often than they pass.

Oscillatory motion with a constant or slowly monotonously increasing amplitude, which is larger than the cell size, is the hallmark of the Fibronectin deposition effect on cell trajectories (31). We did not observe oscillations of this type in our experiments. Oscillations with constant amplitude in our trajectories had amplitudes close to cell size and thus cannot be distinguished from state SO and were classified as such.

Bolado-Carrancio et al. (32) investigate the coordination of the Rho GTPase network activity across MDA-MB-231 cells. The mainly experimental study also simulates a mathematical model and is closely related to Holmes et al. (33). Holmes et al. (33) favour an oscillation mechanism with bistability resulting from the Rac1-RhoA-antagonism. Integrin signals via paxillin, FAK and Src to activate Rac1 and suppresses RhoA (34, 35). RhoA and Rac1 are additionally connected in a signalling network also comprising DIA, ROCK and PAK (32). This network acts in a way that in the end RhoA and Rac1 mutually suppress their activity to a degree controlled by the presence of DIA and/or ROCK. This double negative feedback causes the bistability. Holmes et al. (33) introduced a slow negative feedback from interaction with ECM due to area changes of lamellipodia modulating integrin signalling. The slow feedback turns the bistability into oscillations. Conservation of total Rac1 and RhoA turned out to be essential for robust agreement of RhoA/Rac1 dynamics with experiments (32, 33, 36). The Rac1-RhoA-antagonism with conservation of total Rac1 and RhoA produces anti-phase oscillations (33, 36), as systems with essential feedback on the basis of resource limitations or conservation have the tendency to do. Park et al. state “Conservation of the total amount of small GTPases in a cell effectively leads to a double negative feedback between the front and the back of the cell, preventing simultaneous high activation in both front and back cellular compartments.” (36). We do not observe strictly antiphase or in-phase oscillations but rather a continuum of phase relations.

Bolado-Carrancio et al. (32) report leading edge Rac1-mediated oscillations with a period in the 30-60 s range at the front protrusion. They suggest the back to be most of the time in a state with high RhoA activity and activated ROCK. That state is interrupted by waves of high Rac1 activity from the front arriving with a period of about 4-5 min at the back (their Figure 5-figure supplement 1C, control). Bolado-Carrancio et al. suggest these waves to cause periodic back retractions.

The cell movement cycle is described by the authors in the introduction as “The leading edge protrudes and retracts multiple times, until the protrusions, known as lamellipodia, are stabilised by adhering to the extracellular matrix (Ridley, 2001). Subsequently, the cell back detaches and contracts allowing the cell body to be pulled toward the front.” The cell movement cycle takes about 45 min (Bolado-Carrancio et al. (32) text and movie 2). Hence, on average one in ten wave arrivals causes retraction of the back.

The retraction mechanism is based on myosin. It is explained as “Because of the oscillations, zones of low Rac1 activities emerge, which give rise to high RhoA-GTP that interacts with ROCK and leads to the back retraction (Video 1). Subsequently, RhoA returns to its initial high stable activity, and the dynamic pattern of RhoA-GTP and Rac1-GTP over the entire cell returns to its initial state. These model simulations could plausibly explain how the different GTPase dynamics at the cell front and back are coordinated to enable successful cell migration.” Here, oscillations at the back are meant and are also called ‘adhesion-retraction cycle at the back’. Details on how the Rac1-activity at the back causes retraction but the state with high ROCK activity activating myosin does not are not provided. The reasoning is, where Rac1 is low, RhoA is high, activates ROCK and this in turn phosphorylates the myosin light chain causing contraction. However, the areas of low Rac1 during the waves are much smaller than during the stationary state and therefore contraction should be weaker. Also and consequently, there should be no retractions with Blebbistatin, if we face this mechanism. Our finding that oscillations and thus protrusion retractions are observed with Blebbistatin applied is difficult to reconcile with the myosin based retraction mechanisms suggested in ref. (32). We found myosin’s role in formation of adhered structures to be more important than as a contractile driver of F-actin flow and protrusion retraction (1).

We consider the likelihood that the oscillations we observe obey the GTPase-mechanism by looking at time scales. The oscillations that we observe at the back have average periods in the range from 15 min to 30 min, i.e. are slower than the Rac1-wave period and faster than the movement cycle reported by Bolado-Carrancio et al. We do not observe exclusively antiphase oscillations, as the GTPase-mechanism suggests, but a whole range of phase relations. We find similar time scale differences when comparing our observations to the RhoA-RhoGDI-based pacemaker mechanism suggested by Tkachenko et al. (37) acting on a time scale of about 100 s. Interestingly, interrupting the pacemaker function by inhibiting its negative feedback to RhoA by inhibiting PKA increased the typical time scale to about 10 min.

S14 SUPPLEMENTAL MOVIES

Completing the supplemental material are 6 movies (S1-S6). They are phase-contrast movies of single MDA-MB-231 cells migrating on a Fibronectin lane. The nuclear marker H2B mCherry is shown in magenta. The movies correspond to Fig.1, panels A-F. The clock’s format is h:min. Images were taken every 30s, playback speed is 150 min/s for movie S1 and 15 min/s for movies S2-S6. Scale bars equal 10 μm.

REFERENCES

1. Schreiber, C., B. Amiri, J. C. J. Heyn, J. O. Rädler, and M. Falcke, 2021. On the adhesion–velocity relation and length adaptation of motile cells on stepped fibronectin lanes. *Proceedings of the National Academy of Sciences* 118. https://www.pnas.org/content/118/4/e2009959118.

2. Coué, M., S. L. Brenner, I. Spector, and E. D. Korn, 1987. Inhibition of actin polymerization by latrunculin A. *FEBS letters* 213:316–318.

3. Hennig, K., I. Wang, P. Moreau, L. Valon, S. DeBeco, M. Coppey, Y. A. Miroshnikova, C. Albiges-Rizo, C. Favard, R. Voituriez, and M. Balland, 2020. Stick-slip dynamics of cell adhesion triggers spontaneous symmetry breaking and directional migration of mesenchymal cells on one-dimensional lines. *Science Advances* 6:eaau5670. https://advances.sciencemag.org/content/advances/6/1/eaau5670.full.pdfhttps://www.ncbi.nlm.nih.gov/pmc/articles/PMC6941913/pdf/aau5670.pdf.

4. Schreiber, C., F. J. Segerer, E. Wagner, A. Roidl, and J. O. Rädler, 2016. Ring-Shaped Microlanes and Chemical Barriers as a Platform for Probing Single-Cell Migration. *Scientific Reports* 6:26858.

5. Jurado, C., J. R. Haserick, and J. Lee, 2005. Slipping or Gripping? Fluorescent Speckle Microscopy in Fish Keratocytes Reveals Two Different Mechanisms for Generating a Retrograde Flow of Actin. *Mol Biol Cell* 16:507–518.

6. Renkawitz, J., K. Schumann, M. Weber, T. Lämmermann, H. Pflicke, M. Piel, J. Polleux, J. P. Spatz, and M. Sixt, 2009. Adaptive force transmission in amoeboid cell migration. *Nature Cell Biology* 11:1438–1443.

7. Maiuri, P., J.-F. Rupprecht, S. Wieser, V. Ruprecht, O. Bénichou, N. Carpi, M. Coppey, S. D. Beco, N. Gov, C.-P. Heisenberg, C. L. Crespo, F. Lautenschlaeger, M. L. Berre, A.-M. Lennon-Dumenil, M. Raab, H.-R. Thiam, M. Piel, M. Sixt, and R. Voituriez, 2015. Actin Flows Mediate a Universal Coupling between Cell Speed and Cell Persistence. *Cell* 161:374–386. http://www.sciencedirect.com/science/article/pii/S0092867415001804.

8. McGrath, J. L., N. J. Eungdamrong, C. I. Fisher, F. Peng, L. Mahadevan, T. J. Mitchison, and S. C. Kuo, 2003. The Force-Velocity Relationship for the Actin-Based Motility of Listeria monocytogenes. *Curr Biol* 13:329 – 332.

9. Koseki, K., D. Taniguchi, S. Yamashiro, H. Mizuno, D. Vavylonis, and N. Watanabe, 2019. Lamellipodium tip actin barbed ends serve as a force sensor. *Genes to Cells* 24:705–718.

10. Peskin, C., G. Odell, and G. Oster, 1993. Cellular motions and thermal fluctuations: the Brownian ratchet. *Biophys J* 65:316 – 324.

11. Bieling, P., J. Weichsel, R. McGorty, P. Jreij, B. Huang, D. A. Fletcher, R. D. Mullins, et al., 2016. Force feedback controls motor activity and mechanical properties of self-assembling branched actin networks. *Cell* 164:115–127.

12. Dolati, S., F. Kage, J. Mueller, M. Müsken, M. Kirchner, G. Dittmar, M. Sixt, K. Rottner, and M. Falcke, 2018. On the relation between filament density, force generation, and protrusion rate in mesenchymal cell motility. *Molecular Biology of the Cell* 29:2674–2686.

13. Mueller, J., G. Szep, M. Nemethova, I. de Vries, A. D. Lieber, C. Winkler, K. Kruse, J. V. Small, C. Schmeiser, K. Keren, R. Hauschild, and M. Sixt, 2017. Load Adaptation of Lamellipodial Actin Networks. *Cell* 171:188 – 200.e16.

14. Dickinson, R. B., and D. L. Purich, 2002. Clamped-Filament Elongation Model for Actin-Based Motors. *Biophys J* 82:605–617.

15. Mogilner, A., and G. Oster, 2003. Force Generation by Actin Polymerization II: The Elastic Ratchet and Tethered Filaments. *Biophys J* 84:1591–1605.

16. Trichet, L., O. Campàs, C. Sykes, and J. Plastino, 2007. VASP Governs Actin Dynamics by Modulating Filament Anchoring. *Biophys J* 92:1081–1089.

17. Enculescu, M., A. Gholami, and M. Falcke, 2008. Dynamic regimes and bifurcations in a model of actin-based motility. *Physical Review E* 78:031915.

18. Motahari, F., and A. E. Carlsson, 2019. Thermodynamically consistent treatment of the growth of a biopolymer in the presence of a smooth obstacle interaction potential. *Phys. Rev. E* 100:042409.

19. Gholami, A., J. Wilhelm, and E. Frey, 2006. Entropic forces generated by grafted semiflexible polymers. *Phys Rev E* 74:041803.

20. Zimmermann, J., C. Brunner, M. Enculescu, M. Goegler, A. Ehrlicher, J. Käs, and M. Falcke, 2012. Actin Filament Elasticity and Retrograde Flow Shape the Force-Velocity Relation of Motile Cells. *Biophys J* 102:287 – 295.

21. Gardel, M. L., B. Sabass, L. Ji, G. Danuser, U. S. Schwarz, and C. M. Waterman, 2008. Traction stress in focal adhesions correlates biphasically with actin retrograde flow speed. *J Cell Biol* 183:999–1005.

22. Aratyn-Schaus, Y., and M. L. Gardel, 2010. Transient Frictional Slip between Integrin and the ECM in Focal Adhesions under Myosin II Tension. *Current Biology* 20:1145–1153. <GotoISI>://WOS:000280024300021.

23. Li, Y., P. Bhimalapuram, and A. R. Dinner, 2010. Model for how retrograde actin flow regulates adhesion traction stresses. *Journal of Physics: Condensed Matter* 22:194113. https://doi.org/10.1088%2F0953-8984%2F22%2F19%2F194113.

24. Barnhart, E., K.-C. Lee, G. M. Allen, J. A. Theriot, and A. Mogilner, 2015. Balance between cell-substrate adhesion and myosin contraction determines the frequency of motility initiation in fish keratocytes. *Proceedings of the National Academy of Sciences* 112:5045–5050. https://www.pnas.org/doi/abs/10.1073/pnas.1417257112.

25. Evans, E., 2001. Probing the relation between force - lifetime - and chemistry in single molecular bonds. *Annual Review of Biophysics and Biomolecular Structure* 30:105–128.

26. Craig, E. M., J. Stricker, M. Gardel, and A. Mogilner, 2015. Model for adhesion clutch explains biphasic relationship between actin flow and traction at the cell leading edge. *Physical Biology* 12. <GotoISI>://WOS:000361836300003.

27. Allard, J., and A. Mogilner, 2013. Traveling waves in actin dynamics and cell motility. *Current opinion in cell biology* 25:107–115.

28. Zimmermann, J., M. Enculescu, and M. Falcke, 2010. Leading edge - gel coupling in lamellipodium motion. *Phys Rev E* 82:051925.

29. Prass, M., K. Jacobson, A. Mogilner, and M. Radmacher, 2006. Direct measurement of the lamellipodial protrusive force in a migrating cell. *J Cell Biol* 174:767–772.

30. Heinemann, F., H. Doschke, and M. Radmacher, 2011. Keratocyte Lamellipodial Protrusion Is Characterized by a Concave Force-Velocity Relation. *Biophys J* 100:1420 – 1427.

31. d'Alessandro, J., A. Barbier-Chebbah, V. Cellerin, O. Benichou, R. M. Mège, R. Voituriez, and B. Ladoux, 2021. Cell migration guided by long-lived spatial memory. *Nature Communications* 12:4118. https://doi.org/10.1038/s41467-021-24249-8.

32. Bolado-Carrancio, A., O. S. Rukhlenko, E. Nikonova, M. A. Tsyganov, A. Wheeler, A. Garcia-Munoz, W. Kolch, A. von Kriegsheim, and B. N. Kholodenko, 2020. Periodic propagating waves coordinate RhoGTPase network dynamics at the leading and trailing edges during cell migration. *eLife* 9:e58165. https://doi.org/10.7554/eLife.58165.

33. Holmes, W. R., J. Park, A. Levchenko, and L. Edelstein-Keshet, 2017. A mathematical model coupling polarity signaling to cell adhesion explains diverse cell migration patterns. *PLOS Computational Biology* 13:1–22. https://doi.org/10.1371/journal.pcbi.1005524.

34. Harburger, D. S., and D. A. Calderwood, 2009. Integrin signalling at a glance. *Journal of Cell Science* 122:159–163. https://jcs.biologists.org/content/122/2/159.

35. Warner, H., B. J. Wilson, and P. T. Caswell, 2019. Control of adhesion and protrusion in cell migration by Rho GTPases. *Current Opinion in Cell Biology* 56:64 – 70. http://www.sciencedirect.com/science/article/pii/S095506741830111X, cell Architecture.

36. Park, J., W. R. Holmes, S. H. Lee, H.-N. Kim, D.-H. Kim, M. K. Kwak, C. J. Wang, L. Edelstein-Keshet, and A. Levchenko, 2017. Mechanochemical feedback underlies coexistence of qualitatively distinct cell polarity patterns within diverse cell populations. *Proceedings of the National Academy of Sciences* 114:E5750–E5759. https://www.pnas.org/content/114/28/E5750.

37. Tkachenko, E., M. Sabouri-Ghomi, O. Pertz, C. Kim, E. Gutierrez, M. Machacek, A. Groisman, G. Danuser, and M. H. Ginsberg, 2011. Protein kinase A governs a RhoA-RhoGDI protrusion-retraction pacemaker in migrating cells. *Nat Cell Biol* 13:660–667.